Cardiolipin deficiency disrupts CoQ redox state and induces steatohepatitis

Marisa J. Brothwell,[1,2] Guoshen Cao (曹国燊),[1,3] J. Alan Maschek,[1,2,4] Annelise M. Poss,[1,2] Alek D. Peterlin,[1,2] Liping Wang (汪立平),[1,2] Talia B. Baker,[5,6] Justin L. Shahtout,[1,7] Piyarat Siripoksup,[1,7] Quentinn J. Pearce,[4] Jordan M. Johnson,[1,2] Fabian M. Finger,[8,9] Alexandre Prola,[10] Sarah A. Pellizzari,[3,11] Gillian L. Hale,[5,11] Allison M. Manuel,[4] Shinya Watanabe (渡邉真也),[1,2] Edwin R. Miranda,[1,2,12] Kajsa E. Affolter,[5,10] Trevor S. Tippetts,[1,2] Linda S. Nikolova,[13] Ran Hee Choi (崔蘭熙),[1,2,12] Stephen T. Decker,[1,2,12] Mallikarjun Patil,[1,2,12] J. Leon Catrow,[4] William L. Holland,[1,2,3,12] Sara M. Nowinski,[14] Daniel S. Lark,[15,16] Kelsey H. Fisher-Wellman,[17] Patrice N. Mimche,[18] Kimberley J. Evason,[5,11] James E. Cox,[1,3,4] Scott A. Summers,[1,2,3,5,12] Zach Gerhart-Hines,[8,9] Katsuhiko Funai (船井勝彦),*[1,2,3,5,7,12]

[1]Diabetes & Metabolism Research Center; University of Utah; Salt Lake City, UT; USA.
[2]Department of Nutrition and Integrative Physiology; University of Utah; Salt Lake City, UT; USA.
[3]Department of Biochemistry; University of Utah; Salt Lake City, UT; USA.
[4]Metabolomics Core Research Facility; University of Utah; Salt Lake City, UT; USA.
[5]Huntsman Cancer Institute; University of Utah, Salt Lake City, UT; USA.
[6]Division of Transplantation and Advanced Hepatobiliary Surgery, Department of Surgery; University of Utah; Salt Lake City, UT; USA.
[7]Department of Physical Therapy and Athletic Training; University of Utah; Salt Lake City, UT; USA.

[8]Novo Nordisk Foundation Center for Basic Metabolic Research; University of Copenhagen; Copenhagen; DK.

[9]Center for Adipocyte Signaling (ADIPOSIGN); University of Southern Denmark; Odense; DK.

[10]Laboratory of Fundamental and Applied Bioenergetics; University of Grenoble Alpes, Inserm U1055; Grenoble; FR.

[11]Department of Pathology; University of Utah; Salt Lake City, UT; USA.

[12]Molecular Medicine Program; University of Utah; Salt Lake City, UT; USA.

[13]Electron Microscopy Core Facility; University of Utah; Salt Lake City, UT; USA.

[14]Department of Metabolism and Nutritional Programming; Van Andel Institute; Grand Rapids, MI; USA.

[15]College of Health and Human Sciences; Colorado State University; Fort Collins, CO; USA.

[16]Columbine Health Systems Center for Healthy Aging; Colorado State University; Fort Collins, CO; USA

[17]Department of Cancer Biology, Wake Forest University School of Medicine; Atrium Health Wake Forest Baptist Comprehensive Cancer Center; Winston-Salem, NC; USA.

[18]Departments of Dermatology and Medicine; Division of Gastroenterology and Hepatology, Indiana University School of Medicine; Indianapolis, IN; USA.

*Lead Contact

Correspondence:

Katsuhiko Funai, Ph.D.

kfunai@health.utah.edu

Summary

Metabolic dysfunction-associated steatotic liver disease (MASLD) is a progressive disorder marked by lipid accumulation, leading to steatohepatitis (MASH). A key feature of the transition to MASH involves oxidative stress resulting from defects in mitochondrial oxidative phosphorylation (OXPHOS). Here, we show that pathological alterations in the lipid composition of the inner mitochondrial membrane (IMM) directly instigate electron transfer inefficiency to promote oxidative stress. Specifically, cardiolipin (CL) was downregulated across four mouse models of MASLD. Hepatocyte-specific CL synthase knockout (CLS-LKO) led to spontaneous MASH with elevated mitochondrial electron leak. Loss of CL interfered with the ability of coenzyme Q (CoQ) to transfer electrons, promoting leak primarily at sites II_F and III_{Q0}. Data from human liver biopsies revealed a highly robust correlation between mitochondrial CL and CoQ, co-downregulated with MASH. Thus, reduction in mitochondrial CL promotes oxidative stress and contributes to pathogenesis of MASH.

Introduction

Metabolic-dysfunction associated steatotic liver disease (MASLD) is a growing global health concern with an increasing prevalence that parallels the rise in obesity.[1] In the United States, annual medical costs related to MASLD exceed $103 billion.[2] A large portion of patients with MASLD only exhibit steatosis, a silent and relatively benign early stage characterized by lipid accumulation in hepatocytes without hepatocellular inflammation.[3] Steatosis can then progress to metabolic-dysfunction associated steatohepatitis (MASH), determined by hepatocyte injury and tissue fibrosis.[4] MASH is the last stage of MASLD that may be reversible, making intervention at this stage particularly important.[3,5] Although extensive clinical and basic research have been conducted in this field, the underlying mechanisms by which fatty liver transitions to MASH remain poorly understood.[6-8]

A defect in mitochondrial function is considered one of the hallmarks of MASLD progression in both mice and humans.[9-12] MASLD is initially associated with an increase in mitochondrial respiratory capacity, followed by a subsequent impairment in oxidative phosphorylation (OXPHOS), and increased production of mitochondrial reactive oxygen species (ROS).[11,13] Mitochondrial ROS is thought to be caused by an inefficient electron transport chain (ETC) that increases the propensity for electron leak. However, the mechanisms by which mitochondrial electron leak promotes MASLD are unknown.

Cardiolipin (CL) is a phospholipid with four acyl chains conjugated to two phosphatidylglycerol moieties linked by another glycerol molecule.[14] CL resides almost exclusively in the inner mitochondrial membrane (IMM), constituting approximately 15–20% of the mitochondrial phospholipids.[15] CL is synthesized by the condensation of phosphatidylglycerol (PG) and cytidine diphosphate-diacylglycerol (CDP-DAG) at the IMM via the enzyme cardiolipin synthase (CLS).[16,17] Structural studies indicate that CL is essential for the activities of OXPHOS

enzymes.[18-22] In non-hepatocytes, decreased CL leads to compromised oxidative capacity,[23,24] impaired membrane potential,[25] and altered cristae morphology.[26] In particular, low CL is associated with increased H_2O_2 production.[27,28]

In this manuscript, we set out to examine the changes in liver mitochondrial lipidome induced by MASH. Mitochondrial CL was downregulated in four mouse models of MASLD. We then performed a targeted deletion of CLS in hepatocytes and studied its effects on liver, mitochondrial bioenergetics, and potential mechanisms that drive these changes.

Results

Mitochondrial cardiolipin levels are decreased in mouse models of MASLD/MASH

Previous research from our lab in non-hepatocytes indicated that mitochondrial phospholipid composition affects OXPHOS electron transfer efficiency to alter electron leak.[15,29,30] MASLD has been shown to alter the total cellular lipidome in liver.[31] However, MASLD may also influence mitochondrial content in the hepatocytes, making it difficult to discern whether these are changes in the lipid composition of mitochondrial membranes and/or changes in cellular mitochondrial density. Thus, we performed liquid chromatography-tandem mass spectrometry (LC-MS/MS) lipidomics specifically on mitochondria isolated from four models of MASLD/MASH (Figure 1). These included: 1) mice given a Western high-fat diet (HFD, Envigo TD.88137) or standard chow diet for 16 weeks (Figure 1A), 2) ob/ob mice or their wildtype littermates at 20 weeks of age (Figure 1B), 3) mice given the Gubra Amylin NASH diet for 30 weeks (GAN, Research Diets D09100310) or standard chow (Figure 1C), 4) mice injected with carbon tetrachloride (CCl_4) or vehicle (corn oil) for 6 weeks (Figure 1D). Importantly, none of these interventions appear to alter the protein abundances of OXPHOS subunits or citrate synthase (Figures 1E, 1F, 1G, and 1H), suggesting that these interventions did not alter mitochondrial

density in hepatocytes. Nevertheless, we performed the mitochondrial lipidomic analyses by quantifying lipids per mg of mitochondrial proteins.

Each intervention appeared to alter different subsets of mitochondrial lipid classes (Figures 1I-L, S1, and S2), as seen with our previous studies in skeletal muscle and brown adipose tissues.[29,30] We take these observations to mean that most physiological interventions induce multiple systemic and local responses that are not mechanistically directly related to the phenotype of interest (e.g., cold exposure or exercise can increase food intake, obesity could affect locomotion and insulation, etc.). Although several phospholipid classes were altered among the four models, strikingly, mitochondrial CL was reduced in all four MASLD/MASH models (Figure 1I-M). Furthermore, PG, an essential substrate for CL synthesis, was significantly increased in all MASLD/MASH models (Figure 1I-M). These changes coincided with decreased transcript levels for CLS (Figure 1N, 1O, 1P, and 1Q). These observations suggest that an insult in CL synthesis may be a key factor to disrupting mitochondrial function in MASLD/MASH.

Hepatocyte-specific deletion of cardiolipin synthase promotes MASH

CL is thought to be exclusively synthesized in the IMM where CLS is localized. To study the role of CL in hepatocytes, we generated mice with hepatocyte-specific knockout of CLS (CLS-LKO for *CLS l*iver *k*nock*o*ut, driven by albumin-Cre) (Figures 2A and 2B), which successfully decreased mitochondrial CL levels (Figure 2C and S3). Consistent with our previous studies in non-hepatocytes, CLS deletion does not completely reduce CL levels to zero, suggesting that CL generated in other tissues may be imported. Our results showed that decreased levels of CL did not significantly impact body weight or composition (Figures 2D and 2E) but resulted in significantly less liver mass (Figure 2F).

We sought to further characterize livers from control and CLS-LKO mice. Histological analyses revealed that CLS deletion was sufficient to promote steatosis (Figure 2G) and fibrosis (Figure 2H) in standard chow-fed and high-fat fed conditions (Figures S4A and S4B). To more comprehensively describe the effects of loss of hepatic CLS on gene expression, we performed RNA sequencing on these livers. CLS deletion increased the expression of 713 genes and decreased 1026 genes (Figure S4C). Pathway analyses revealed that many of the signature changes that occur with MASLD/MASH also occurred with CLS deletion (Figures 2I and S4D). This MASLD/MASH phenotype in our CLS knockout model was further confirmed with an elevation of the liver enzymes AST and ALT (Figures 2J and 2K) as well as increased mRNA levels of inflammatory markers (Figure 2L). We then proceeded to confirm these data by further phenotyping liver tissues from control and CLS-LKO mice.

In steatohepatitis, immune cell populations in the liver become altered to activate pathological immune response.[32] Flow cytometry on livers from control and CLS-LKO mice indicated that the loss of CL promotes a robust classic immune response found in MASH (Figure 2M). cDC2 cells are a broad subset of dendritic cells with specific surface markers (e.g., CD11b, CD172a) that allow them to be distinguished from other dendritic cell populations.[33] This broad population of dendritic cells was not different between control and CLS-LKO mice (Figure 2N). Notably, there was a marked reduction in the Kupffer cell population (Figure 2O) - traditionally involved in maintaining liver homeostasis whose dysfunction can lead to dysregulated immune response.[34] This reduction appears to be counterbalanced by a concomitant increase in Ly6C^{hi} population, which are known to typically go on to become inflammatory monocytes (Figures 2M and 2P). The replacement of Kupffer cells with other inflammatory cell populations suggests a shift towards a more pro-inflammatory environment, which may exacerbate liver injury and promote fibrosis. Nonetheless, the MHC-II cell population and neutrophils were not increased (Figures 2Q and 2R) with neutrophils actually decreased (Figure 2R). The cDC1 cell population was not

different, which is traditionally elevated in response to cytotoxic T cells and might not be directly related to liver fibrosis.[35] Together, these findings suggest that even on a chow diet, CLS-deficient livers exhibit inflammatory cell infiltration, a hallmark often associated with early signs of MASH.

CLS deletion promotes fatty liver but increases mitochondrial respiratory capacity

Hepatocyte lipid accumulation may suggest defects in substrate handling, which is often manifested in systemic substrate handling. Indeed, CLS deletion modestly reduced glucose or pyruvate handling, even in chow-fed conditions (Figures 3A-D). Lipid accumulation in hepatocytes can occur due to an increase in lipogenesis, a decrease in VLDL secretion, or a decrease in β-oxidation. However, mRNA levels for lipogenesis genes trended lower (not higher), and mostly unchanged for VLDL secretion or β-oxidation (Figure 3E, Figure S5A). Circulating triglycerides were not lower in CLS-LKO mice compared to control mice (Figure S5B).

MASLD is known to be associated with reduced mitochondrial oxidative capacity, and such an effect may also occur with CL deficiency to induce lipid accumulation. Indeed, mRNA levels of several genes in the ETC were downregulated with CLS deletion, particularly those associated with structural components of the ETC complexes and the electron carrier CoQ (Figure 3F). Given that CL is located in the IMM where it binds to enzymes involved in OXPHOS,[36-39] we reasoned that the loss of CL could reduce mitochondrial oxidative capacity to promote steatosis. Consistent with subcellular localization of CL, CLS deletion resulted in mitochondria with disorganized membrane structures and poorly developed cristae (Figure 3G). However, mitochondrial density quantified with western blots for respiratory complex subunits and citrate synthase (Figure 3H), as well as mtDNA/nucDNA (Figure 3I), showed no differences in livers from control and CLS-LKO mice. We thus speculated that CL lowers respiratory capacity not by

reducing the total number of mitochondria or OXPHOS respirasomes, but by reducing the activity of respiratory enzymes. To our surprise, CLS deletion increased, rather than decreased, mitochondrial respiration (JO_2), as measured by high-resolution Oroboros respirometry (Figure 3J), using both with Krebs cycle substrates (Figure 3K) as well as fatty acyl substrates (Figure 3L). In fact, the increase in respiration induced by CLS deletion was more pronounced with fatty acyl substrates than with Krebs Cycle substrates. Importantly, these changes occurred in the absence of OXPHOS subunit abundance per unit of mitochondria (Figure 3M), ruling out the possibility that changes in the abundance of respiratory enzymes to contribute to change in respiration. A caveat to these findings is that CLS deletion promotes reduction in respiratory capacity after HFD-feeding (Figures S5C and S5D). However, CLS-LKO mice are steatotic in standard chow-fed condition, indicating that reduced mitochondrial fatty acid oxidation cannot be the cause of steatosis at baseline. The transient increase in respiration followed by its subsequent decrease is reminiscent of what is thought to occur with liver's mitochondrial respiration over the course of MASLD progression.[40]

High-resolution respirometry experiments were performed in isolated mitochondria from hepatocytes by providing exogenous supraphysiological concentrations of substrates. While these assays provide robust measurements of respiratory capacity (the potential of mitochondria), they do not necessarily reflect their endogenous activity. To address this point, we performed stable isotope tracing experiments using uniformly labeled ^{13}C-palmitate in murine hepa1-6 cells with or without CLS knockdown (Figure 4A).[41] Surprisingly, but consistent with the JO_2 data, CLS deletion increased, not decreased, the incorporation of palmitate into TCA intermediates (Figures 4B-D). We also performed a similar tracing experiment using uniformally labeled ^{13}C-glucose (Figure 4E-J, S5E-I) and observed increased labeling towards pyruvate (Figure 4E and 4F), reduced labeling towards lactate and alanine (Figures 4G and S5H), and normal labeling towards TCA intermediates except for reduced labeling towards

succinate (Figure 4H-J, S5I-M). Overall, despite the altered substrate incorporation, a decrease in TCA flux does not appear to account for the steatotic phenotype observed with CLS deletion.

Low hepatic CL induces mitochondrial electron leak at II_F and III_{Q0} sites

Oxidative stress is thought to play a critical role in the transition from MASLD to MASH, wherein sustained metabolic insult leads to hepatocellular injury and collagen deposition resulting in fibrosis.[7] CLS deletion promotes liver fibrosis in standard chow-fed condition (Figures 5A and 2H) and in HFD-fed condition (Figure S4B) that coincided with increased mRNA levels for fibrosis (Figure 5B and 2I). Tissue fibrosis is often triggered by apoptosis, and CLS deletion appeared to activate the caspase pathway (Figures 5C and 5D). How does deletion of CLS, a mitochondrial enzyme that produces lipids for IMM, activate apoptosis? Cytochrome c is an electron carrier that resides in IMM, which shuttles electrons between complexes III and IV.[42] Under normal physiological conditions, cytochrome c is anchored to the IMM by its binding to cardiolipin.[39] During the initiation of intrinsic apoptosis, CL can undergo oxidation and redistribution from the IMM to the outer membrane space (OMM). CL oxidation weakens its binding affinity for cytochrome c, releasing it from the IMM and into the OMM where it signals apoptosis.[13] However, neither mitochondrial nor cytosolic cytochrome c abundance appeared to be influenced by CLS deletion (Figures 5E, 5F, S6A, and S6B).

Mitochondrial ROS has been implicated in apoptosis and fibrosis with MASLD.[43-45] Using high-resolution fluorometry in combination with high-resolution respirometry, we quantified electron leak from liver mitochondria with the assumption that almost all electrons that leak react with molecular O_2 to produce O_2^-. Using recombinant superoxide dismutase, we ensure that all O_2^- produced is converted into H_2O_2, which was quantified with the AmplexRed fluorophore.[46] There were striking increases in mitochondrial electron leak in CLS-LKO mice compared to control mice on both standard chow (Figure 5G) and high-fat diet (Figure S6C). It is noteworthy that

endogenous antioxidant pathways were insufficient to completely suppress oxidative stress induced by CLS deletion (H_2O_2 emission shown in the 1st and 2nd bars in Figure 5G and S6C). We also confirmed that JH_2O_2/JO_2 was elevated with CLS knockdown in mitochondria from murine hepa1-6 cell line (Figure S6D) suggesting that low CL induces oxidative stress in a cell-autonomous manner.

While unknown, CLS may possess an enzymatic activity independent of CL synthesis that may contribute to electron leak. To more conclusively show that the loss of mitochondrial CL contributes to oxidative stress, we supplied exogenous CL to isolated mitochondria by fusing them with small unilamellar vesicles (SUVs) (Figure 5H).[47] Isolated mitochondria from control and CLS-LKO mice were fused with SUVs containing either CL or phosphatidylcholine (PC) (Figures 5I and S6E). Remarkably, reintroducing CL to mitochondria from CLS-LKO mice reduced H_2O_2 production back to baseline, whereas PC had no effect. Thus, loss of CL drives the increased mitochondrial leak observed with CLS deletion.

How does low CL promote mitochondrial electron leak? CL is likely ubiquitous in IMM and can bind to all four respiratory complexes of the ETC.[20,21,36,48] There are four known sites of electron leak in the IMM: 1) quinone-binding site in complex I (I_Q), 2) flavin-containing site in complex I (I_F), 3) succinate-dehydrogenase-associated site in complex II (II_F), and the ubiquinol oxidation site in complex (III_{Qo}) Figure 6). Electron leak at each of these sites can be quantified separately using substrates and inhibitors that restrict electron flow specific to these sites. All of these sites are localized to IMM, suggesting that CL has the potential to increase electron leak in any of these sites. Indeed, quantification of site-specific electron leak demonstrated that CLS deletion essentially increased electron leak in all these sites (Figures 6A, 6B, 6C, and 6D).

Loss of CL promotes inefficiency in coenzyme Q-dependent electron transfer

How does the loss of CL promote electron leak at these sites? We initially addressed whether CL influences the formations of respiratory supercomplexes. Respiratory supercomplexes exist in several combinations of multimers of Complex I, III, IV, and V and are thought to form either transiently or stably to improve electron transfer efficiency.[48,49] CL may play an essential role in the stability of ETC supercomplexes.[50,51] Using blue native polyacrylamide gel electrophoresis followed by subunit-specific western blotting, we investigated supercomplex assembly in isolated hepatic mitochondria from control and CLS-LKO mice (Figures 6E-P). Abundances of supercomplexes associated with CIII (Figure 6L) as well as CV (Figure 6P) were reduced, while singlets for CII (Figure 6J), CIII (Figure 6L), and CIV (Figure 6N) were increased in mitochondria from CLS-LKO mice compared to control mice. Nevertheless, in our opinion, these changes were somewhat underwhelming in that: 1) among ETC, only one of the supercomplexes, one associated with CIII ($I + III_2 + IV_1$), was reduced out of nine total, and 2) the magnitude of the change in supercomplex formation appeared so trivial compared to the magnitude of electron leak that was observed in sites I_F, II_F, and III_{Q0}. Thus, while loss of some CIII supercomplexes may be a contributor, we did not find these data robust enough and reasoned that there was another mechanism by which CL influenced electron transfer efficiency.

Upon re-examining our site-specific electron leak data (Figure 6A-D), we noted that increases in electron leak were greater at sites II_F and III_{Q0}, and that these sites were proximal to coenzyme Q (CoQ). CoQ, like CL, is a lipid molecule (Figure 7A), and we thought it was possible that CL somehow interacts with CoQ to influence its electron transfer efficiency. Using redox mass spectrometry, we measured CoQ levels in whole liver tissues from control and CLS-LKO mice and found no difference in whole liver tissue CoQ levels (Figures S7A-I). However, since CoQ may also be found outside of mitochondria, we performed CoQ redox mass spectrometry in isolated mitochondria fractions of livers from control or CLS-LKO mice. Indeed, oxidized CoQ levels were increased (Figures 7B, S7J, S7L, and S7N) in CLS-LKO mice compared to their

controls. In contrast, reduced forms of CoQ were not lower in CLS-LKO mice compared to control mice (Figures 7C, S7K, S7M, and S7O). These findings indicate how CL deficiency might influence CoQ-dependent electron transfer. First, low CL increased the abundance of oxidized CoQ, but these oxidized CoQ were unable to become reduced at sites I_Q or II_Q. Thus, loss of CL appears to decrease the ability of CoQ to accept electrons, promoting electron leak at I_F, I_Q, and II_F sites. Second, there must be a second defect, as there was a substantial increase in electron leak from site III_{Q0} (Figure 6D). It can be postulated that CoQ must also be less capable of efficiently donating electrons to complex III. This would be consistent with the data that greater oxidized CoQ was observed despite having a normal reduced CoQ level.

Electron leak from site II_F was greater than those observed in sites I_F and I_Q. Data from the stable isotope experiments supports this notion, where CLS deletion reduced labeling of succinate indicating reduced complex II/succinate dehydrogenase (SDH) activity (Figure 4H). Steady-state metabolomics (Figure S7P) also revealed reduced succinate-to-fumarate ratio, suggesting reduced SDH activity (Figures 7D, S7Q, and S7R). Interestingly, in an assay that measures SDH activity in a detergent-containing assay that removes CL, CLS deletion had no effect (Figure 7E). Thus, loss of CL likely influences multiple processes in the ETC to increase mitochondrial ROS production.

CL and CoQ are co-downregulated in liver biopsy samples from MASH patients

We further assessed the relationship between CL and CoQ by assessing their levels in liver samples from patients undergoing liver transplant or resection due to end-stage MASH and/or hepatocellular carcinoma (Table S1). A portion of liver that did not have tumor was isolated and analyzed. Liver samples from patients without MASH, undergoing resection for bening live rumors or metastases, were classified as healthy controls (Figure 7F). Similar to our experiments in mice, we isolated mitochondria from these liver tissues and performed targeted

lipid mass spectrometry to quantify CoQ and CL. These analyses revealed striking decreases in both CL (Figure 7G) and CoQ (Figure 7H) induced by MASH (tissue samples were not large enough to perform CoQ redox mass spectrometry on mitochondria). A Pearson correlation analysis showed a highly robust correlation between the abundances of mitochondrial CL and CoQ (Figure 7I, $R^2 = 0.64$), indicating that the variability in the abundance of CL explains 64% of the variability of the abundance of CoQ. Based on our findings that CL is reduced with MASLD/MASH and that loss of CL influences CoQ electron transfer efficiency, we interpret these findings to mean that loss of CL destabilizes CoQ to increase its turnover.

Discussion

In hepatocytes, disruptions of mitochondrial bioenergetics lead to and exacerbate metabolic-associated steatohepatitis.[52] CL, a key phospholipid in the inner mitochondrial membrane, plays a critical role in mitochondrial energy metabolism.[23] In this manuscript, we examined the role of CL in the pathogenesis of MASLD. In mice and in humans, MASLD/MASH coincided with a reduction in mitochondrial CL levels. Hepatocyte-specific deletion of CLS was sufficient to spontaneously induce MASH pathology, including steatosis and fibrosis, along with shift in immune cell populations towards a more pro-inflammatory profile, all of which occurred in mice given a standard chow diet. Paradoxically, high-resolution respirometry and stable isotope experiments showed that CLS deletion promotes, instead of attenuates, mitochondrial oxidative capacity in a fashion reminiscent of temporal changes that occur with mitochondrial bioenergetics in human MASH.[40] Our principal finding on the role of hepatocyte CL in bioenergetics is that its loss robustly increases electron leak, particularly at complexes II and III. This was likely due to the influence of CL on mitochondrial CoQ, whereby CLS deletion lowered CoQ's ability to efficiently transfer electrons. In humans, mitochondrial CL and CoQ were co-downregulated in MASH patients compared to healthy controls, with a strong correlation (R^2 =

0.64) between CL and CoQ. Together, these results implicate CL as a key regulator of MASH progression, particularly through its effect on CoQ redox state to promote oxidative stress.

How might CL regulate CoQ? CoQ is the main electron transporter between complex I/II and III. CLS deletion in hepatocytes appeared to disrupt CoQ's ability to cycle between its oxidized and reduced forms. There are several ways in which low CL might directly or indirectly influence CoQ's redox state. The primary suspect is CL interacting with complex III, as eight or nine CL molecules are tightly bound to complex III[38] and are thought to be essential to its function.[53] While CL has been found to bind to other respiratory complexes, our data suggest that loss of CL might disproportionately influence complex III. This is also supported by our findings that the loss of CL reduced the formation of complex III-dependent supercomplex, without influencing other supercomplexes. Reduced capacity for complex III to efficiently accept electrons from CoQ might explain the increased electron leak at site III_{Q0} and increased level of oxidized CoQ. Meanwhile, loss of CL also likely influences complex I and II, as CL has also been implicated to bind these complexes.[20,21,36] Complex III dysfunction is unlikely to entirely explain electron leaks at sites I_F, I_Q, and II_F, though it is conceivable that the reduced ability of complex III to accept electrons creates a bottleneck that produces electron leak at other sites, including reverse electron transport at complex I.[54] Conversely, complex I and II are unlikely to be the only primary sites of defect as such defects probably will not promote electron leak at site III_{QO}. Another potential mechanism by which CL influences CoQ redox state is by CL directly interacting with CoQ. As they are both lipid molecules in the IMM, low CL may reduce the lateral diffusability of CoQ between respiratory complexes. Low CL might also indirectly influence CoQ by contributing to changes in membrane properties, distribution of ETC in the cristae, and the cristae architecture.[55] Finally, increased electron leak, regardless of their origin, could have a feed-forward effect by which oxidative stress disrupts redox homeostasis in other components of ETC.

MASH is a progressive liver disease characterized by lipid accumulation, inflammation, and fibrosis in the liver.[56] The progression to MASH involves a complex interplay of metabolic stress, mitochondrial defects, and immune responses that collectively promote hepatocellular injury.[57] Our findings suggest that the low mitochondrial CL level directly induces key pathological features of MASH, including steatosis, fibrosis, and immune cell infiltration, even in the absence of dietary or environmental stressors, such as high-fat diet. When mice were fed a standard chow diet, CLS-LKO mice were more prone to lipid droplet accumulation than control mice. This phenotype was exacerbated when the mice were challenged with a high-fat diet. We primarily interrogated the mitochondrial bioenergetics of standard chow-fed control or CLS-LKO mice. A lower respiration rate would partially explain the lipid droplet accumulation, but to our surprise, CLS deletion increased JO_2 regardless of substrates. Similarly, experiments using uniformly labeled ^{13}C-palmitate or ^{13}C-glucose showed that CLS deletion promoted an overall increase in the flux toward TCA intermediates, particularly for palmitate. CLS deletion did not appear to increase de novo lipogenesis or reduce VLDL secretion. Thus, it is unclear what mechanisms contribute to steatosis induced by CLS deletion.

Liver fibrosis is characterized by the accumulation of excess extracellular matrix components, including type I collagen, which disrupts liver microcirculation and leads to injury.[55] Livers from CLS-LKO mice exhibited more fibrosis compared to control mice, even on a standard chow diet, which was worsened when fed a high-fat diet. Indeed, transcriptomic analyses revealed that CLS deletion activates pathways for fibrosis and degeneration, with many of the collagen isoforms upregulated. In the MASH liver, collagen deposition is accompanied by inflammatory cell infiltrate promoting an overall inflammatory environment. Flow cytometry experiments further confirmed that CLS deletion led to an increase in Ly6C^{hi} cell population, suggesting that

dying resident Kupffer cells are being replaced by Ly6C^{hi} monocytes in the livers of CLS-LKO mice.[33]

Early in the MASLD disease progression, mitochondria adapt to the increased energy demands by increasing their respiratory capacity. In the later stages of disease progression to MASH, mitochondrial respiration diminishes.[58] This pattern was reminiscent of our observations in the CLS-LKO mice. Livers from CLS-LKO mice fed a standard chow diet exhibited greater respiratory capacity compared to that of control mice. Conversely, livers from CLS-LKO mice on a high-fat diet exhibited lower respiratory capacity compared to that of control mice. We interpret these findings to suggest that liver mitochondria in chow-fed CLS-LKO mice are more representative of early stage of MASLD, while high-fat-diet fed CLS-LKO mice resemble later stages of MASLD.

In non-hepatocytes, low CL levels have been linked to electron leak in the context of a deficiency of the tafazzin gene, a CL transacylase, whose mutation promotes Barth syndrome.[15,26,59,60] Paradoxically, we previously showed that CLS deletion in brown adipocytes does not increase electron leak.[30] It is important to note that CLS deletion in our current or previous study does not completely eliminate CL (likely due to an extracellular source). We do not believe that CL is dispensable for efficient electron transfer in adipocytes. Rather, due to unclear mechanisms, different cell types likely exhibit varying tolerances to low CL influencing their bioenergetics, with brown adipocytes appearing more tolerant than hepatocytes. Regardless, electron leak was elevated with CLS deletion in both standard chow and high-fat diet-fed conditions. These observations mirror what has been shown in MASLD progression.[61] The effect of CLS deletion on electron leak was due to reduced CL levels, as the reintroduction of cardiolipin via SUVs completely rescued the electron leak.

CL is reported to be essential for the formation and stability of supercomplexes.[14,22,50,51] CL has a distinctive conical shape with four fatty acyl chains, which allows it to create a highly curved membrane environment in the IMM, promoting close packing of protein complexes that likely facilitates supercomplex formation.[50] CL also directly interacts with various subunits of the ETC complexes through electrostatic interactions, which help stabilize the supercomplexes by anchoring them together in a specific spatial orientation to optimize electron flow.[49] Somewhat surprisingly, liver-specific deletion of CLS only resulted in a lower abundance of one of many supercomplexes associated with CIII ($I+III_2+IV_1$) as well as the CV multimer (V_n). Because CLS deletion did not completely deplete CL, we interpret these findings to mean that $I+III_2+IV_1$ and V_n supercomplexes are particularly sensitive to the reduced CL level in hepatocytes.

In our study, we observed a striking correlation between CL levels and CoQ in human liver samples from healthy/MASH patients (R_2 of 0.64). In contrast, low mitochondrial CL induced by CLS deletion coincided with a greater mitochondrial CoQ content in CLS-LKO mice compared to controls. These data likely suggest that acute and robust reduction in CLS or CL level might trigger a compensatory CoQ production in mice. Conversely, because the samples from healthy/MASH patients were from those who had HCC, MASH samples likely came from subjects that had suffered from years of MASLD pathology. In those samples, where reduction in CL was quantitatively modest compared to what was induced with CLS knockout, CoQ might have gradually decreased coincidental to the decrease in CL. Regardless of these differences in mice and humans, it is clear that there is a relationship between CL and CoQ that is worth further exploration.

In conclusion, our findings identify a critical role for CL in regulating CoQ redox state to promote oxidative stress. In both mice and humans, MASLD is associated with a decrease in hepatic mitochondrial CL, suggesting that low CL may be the cause of the obligatory increase in

oxidative stress known to occur with MASLD progression. We further link CL deficiency to increased electron leak at Complexes II and III as sites that likely interact with CoQ to promote oxidative stress. We believe that these bioenergetic changes underlie the pathogenesis of MASLD, as CL deletion was sufficient to cause steatosis, fibrosis, and inflammation, phenocopying many changes that occur with MASLD/MASH progression. Further research will be needed to fully uncover how CL regulates CoQ, and to test whether rescuing the CL/CoQ axis might be effective in treating patients with MASLD/MASH.

Acknowledgements

This research was supported by National Institutes of Health (NIH) grants DK127979, GM144613, DK107397, AG074535 (to KF); DK127603 (to AMP), DK130555 (to ADP); HL170575, DK112826 (to WLH); GM151245 (to SMN), CA278803 (to KHF-W); DK128819, DK115991 (to PNM); CA222570 (to KJE); CA272529, DK130296, DK131609 (to SAS); DK091317 (to MJB, TST, STD), by American Heart Association grants 915674 (to PS) and 19PRE34380991 (to JMJ), by European Research Council (ERC) under the European Union's Horizon 2020 Research and Innovation Programme (Starting Grant aCROBAT agreement no. 639382 to ZGH), by Damon Runyon Cancer Research Foundation (Damon Runyon-Rachleff Innovation Award DR 61-20 to KJE), and by the Huntsman Cancer Foundation. The University of Utah Metabolomics Core Facility is supported by NIH S10 OD016232, S10 OD021505, and U54 DK110858. Research reported in this publication utilized the Huntsman Cancer Institute Biorepository and Molecular Pathology Shared Resources supported by NCI/NIH P30 CA042014. We thank Nikita Abraham and Diana Lim (University of Utah Molecular Medicine Program) for assistance with figures.

STAR★Methods

Lead contact

Further information and requests for resources and reagents should be directed to and will be fulfilled by the lead contact, Katsuhiko Funai (kfunai@health.utah.edu).

Materials availability

Plasmids utilized by this study are available from Sigma Aldrich. Mouse lines generated by this study may be available at personal request from the lead contact. No new reagents were created or used by this study.

Data and code availability

The data generated by this study including all images, figures, and datasets, is available upon request to the lead contact, Dr. Katsuhiko Funai. Similarly, any additional information necessary to reanalyze datasets is also available upon request. Code for RNA sequencing can be retrieved upon request.

Experimental model and subject details

Human participants

De-identified liver samples were acquired from the University of Utah Biorepository and Molecular Pathology Shared Resource from patients undergoing liver transplantation or resection due to end-stage liver disease and/or liver tumor(s). All patients were classified to their respective diagnosis by a pathologist at the time of initial collection. The diagnosis for individual tissue samples was confirmed by a pathologist based on histology review of formalin-fixed, paraffin-embedded sections takes from the same location as the tissue analyzed by targeted lipid mass spectrometry.

Mice

All mice (male and female) used in this study were bred onto C57BL/6J background. CLS-LKO mice were generated by crossing the CLS conditional knockout (CLScKO$^{+/+}$) generously donated by Dr. Zachary Gerhart-Hines (University of Copenhagen) with mice heterozygous for Albumin promotor Cre (Alb-Cre$^{+/-}$) to produce liver-specific deletion of the CLS gene (CLScKO$^{+/+}$, Alb-Cre$^{+/-}$) or control (CLScKO$^{+/+}$, no Cre) mice. CLScKO$^{+/+}$ mice harbor loxP sites that flank exon 4 of the CLS gene. For high-fat diet studies, 8 wk CLS-LKO and their respective controls began high-fat diet (HFD, 42% fat, Envigo TD.88137) feeding for 8 wks. Mice were fasted 4 hours and given an intraperitoneal injection of 80 mg/kg ketamine and 10 mg/kg xylazine prior to terminal experiments and tissue collection. All animal experiments were performed with the approval of the Institutional Animal Care and Use Committees at the University of Utah.

Cell lines

Hepa 1-6 murine hepatoma cells were grown in high-glucose DMEM (4.5 g/L glucose, with L-glutamine; Gibco 11965-092) supplemented with 10% FBS (heat-inactivated, certified, US origin; Gibco 10082-147), and 0.1% penicillin-streptomycin (10,000 U/mL; Gibco 15140122). For lentivirus-mediated knockdown of CLS, CLS expression was decreased using the pLKO.1 lentiviral-RNAi system. Plasmids encoding shRNA for mouse *Crls1* (shCLS: TRCN0000123937) was obtained from MilliporeSigma. Packaging vector psPAX2 (ID 12260), envelope vector pMD2.G (ID 12259), and scrambled shRNA plasmid (SC: ID 1864) were obtained from Addgene. HEK293T cells in 10 cm dishes were transfected using 50 µL 0.1% polyethylenimine, 200 µL, 0.15 M sodium chloride, and 500 µL Opti-MEM (with HEPES, 2.4 g/L sodium bicarbonate, and l-glutamine; Gibco 31985) with 2.66 µg of psPAX2, 0.75 µg of pMD2.G, and 3

μg of either scrambled or *Crls1* shRNA plasmid. Cells were selected with puromycin throughout differentiation to ensure that only cells infected with shRNA vectors were viable.

Method details

Body composition

To assess body composition, mice were analyzed using a Bruker Minispec NMR (Bruker, Germany) 1 week prior to terminal experiments. Body weights were measured and recorded immediately prior to terminal experiments.

RNA quantification

For quantitative polymerase chain reaction (qPCR) experiments, mouse tissues were homogenized in TRIzol reagent (Thermo Fisher Scientific) and RNA was isolated using standard techniques. The iScript cDNA Synthesis Kit was used to reverse transcribe total RNA, and qPCR was performed with SYBR Green reagents (Thermo Fisher Scientific). Pre-validated primer sequences were obtained from mouse primer depot (https://mouseprimerdepot.nci.nih.gov/). All mRNA levels were normalized to RPL32. For RNA sequencing, liver RNA was isolated with the Direct-zol RNA Miniprep Plus kit (Zymo Cat#: R2070). RNA library construction and sequencing were performed by the High-Throughput Genomics Core at the Huntsman Cancer Institute, University of Utah. RNA libraries were constructed using the NEBNext Ultra II Directional RNA Library Prep with rRNA Depletion Kit (human, mouse rat). Sequencing was performed using the NovaSeq S4 Reagent Kit v1.5 150x150 bp Sequencing with >25 million reads per sample using adapter read 1: AGATCGGAAGAGCACACGTCTGAACTCCAGTCA and adapter read 2: AGATCGGAAGAGCGTCGTGTAGGGAAAGAGTGT. Pathway analyses were performed by the Bioinformatics Core at the Huntsman Cancer Institute, University of Utah using the Reactome

Pathway Database. For differentially expressed genes, only transcripts with Padj < 0.05 and baseMean > 100 are included.

DNA isolation and quantitative PCR

Genomic DNA for assessments of mitochondrial DNA (mtDNA) was isolated using a commercially available kit according to the manufacturer's instructions (69504, Qiagen). Genomic DNA was added to a mixture of SYBR Green (Thermo Fisher Scientific) and primers. Sample mixtures were pipetted onto a 3840well plate and analyzed with QuantStudio 12K Flex (Life Technologies). The following primers were used: mtDNA fwd, TTAAGA-CAC-CTT-GCC-TAG-CCACAC; mtDNA rev, CGG-TGG-CTG-GCA-CGA-AAT-T; nucDNA fwd, ATGACG-ATA-TCG-CTG-CGC-TG; nucDNA rev, TCA-CTT-ACC-TGGTGCCTA-GGG-C.

Western blot analysis

For whole liver lysate, frozen liver was homogenized in a glass homogenization tube using a mechanical pestle grinder with homogenization buffer (50 mM Tris pH 7.6, 5 mM EDTA, 150 mM NaCl, 0.1% SDS, 0.1% sodium deoxycholate, 1% triton X-100, and protease inhibitor cocktail). After homogenization, samples were centrifuged for 15 min at 12,000 × g. Protein concentration of supernatant was then determined using a BCA protein Assay Kit (Thermo Scientific). Equal protein was mixed with Laemmeli sample buffer and boiled for 5 mins at 95°C for all antibodies except for OXPHOS cocktail antibody (at room temp for 5 mins), and loaded onto 4–15% gradient gels (Bio-Rad). Transfer of proteins occurred on a nitrocellulose membrane and then blocked for 1 hr. at room temperature with 5% bovine serum albumin in Tris-buffered saline with 0.1% Tween 20 (TBST). The membranes were then incubated with primary antibody (see Key Resource table), washed in TBST, incubated in appropriate secondary antibodies, and washed in TBST. Membranes were imaged utilizing Western

Lightning Plus-ECL (PerkinElmer) and a FluorChem E Imager (Protein Simple). For isolated mitochondria, identical procedures were taken with equal protein of mitochondrial preps.

Single cell preparation of liver tissue for flow cytometry

After mice were euthanized using isoflurane, blood was collected by cardiac puncture, the abdomen was exposed and the liver collected, rinse with PBS and weighed. Liver was subsequently transferred in approximately 3ml of serum-free RPMI-1640 containing Collagenase D (10mg/ml; Sigma) and DNase (1mg/ml; Sigma) and incubated in a rocking platform for 45 min at 37°C. The liver extract was mashed through a 70µm filter, the cell re-suspended in RPMI-1640 containing 10% FBS and centrifuged at 1600 rpm for 5 min. The supernatant was discarded and the pellet re-suspended in approximately 4 ml of 70% Percoll, then transferred in 15 ml conical tube, carefully overlay with 4 ml of 30% Percoll and centrifuged 1600 rpm for 25 min with the brake turned off. The non-parenchymal cells suspension from the Percoll interface were removed and mixed with 10 mL of RPMI-1640 containing 10% FBS and the cells were centrifuged at 1600 rpm for 5 min. Red blood cells (RBC) were removed from the pelleted single cell suspensions of livers non-parenchymal cells by incubation in an ammonium chloride -based 1x RBC lysis buffer (Thermofisher, eBioscience). The cells were again pelleted and mixed with FACS buffer (2% BSA, 2mM EDTA in PBS), then stained with Zombie-NIR viability dye (BioLegend) per manufacturer's instructions to discriminate live vs dead cells. To prevent non-specific Fc binding, the cells were incubated with Fc Block (anti-mouse CD16/32, clone 93, Biolegend) for 15 min followed by the indicated antibodies cocktail for 60 min in the dark on ice: CD45 (FITC, clone S18009F, Biolegend), CD11b (BVC421, clone M1/70, Biolegend), F4/80 (APC, clone BM8, Biolegend), TIM4 (PerCP/Cy5.5, clone RMT4-54, Biolegend), Ly6C (PE, clone HK1.4, Biolegend), MHCII (BV605, clone M5/114.15.2, Biolegend), CD11c (BV785, clone N418, Biolegend) and Ly6G (PE/Cy7, clone 1A8, Biolegend). After surface staining, cells were fixed with a paraformaldehyde-based fixation buffer (BioLegend).

Flow cytometric acquisition was performed on a BD Fortessa X20 flow cytometer (BD Biosciebces) and data analyzed using FlowJo software (Version 10.8.1; Tree Star Inc).

Glucose tolerance test

Intraperitoneal glucose tolerance tests were performed by injection of 1 mg glucose per gram body mass at least 6 days prior to sacrifice. Mice were fasted for 4 hours prior glucose injection. Blood glucose was measured 30 minutes before glucose injection and at 0, 15, 30, 60, 90, and 120 minutes after injection via tail bleed with a handheld glucometer (Bayer Contour 7151H).

Pyruvate tolerance test

Pyruvate tolerance tests were performed by injection of 2 mg pyruvate per gram of body mass in PBS adjusted to pH 7.3-7.5 at least 6 days prior to sacrifice. Blood glucose was measured 30 minutes before pyruvate injection and at 0, 15, 30, 45, 60, 75, 90, 105, and 120 minutes after injection via tail bleed with a handheld glucometer (Bayer Contour 7151H).

Electron microscopy

To examine mitochondrial ultrastructure and microstructures, freshly dissected liver tissues from CLS-LKO and their controls were sectioned into ≈2 mm pieces and processed by the Electron Microscopy Core at University of Utah. To maintain the ultrastructure of the tissue via irreversible cross-link formation, each section was submerged in fixative solution (1% glutaraldehyde, 2.5% paraformaldehyde, 100 mM cacodylate buffer pH 7.4, 6 mM CaCl2, 4.8% sucrose) and stored at 4°C for 48 hours. Samples then underwent 3 × 10-minute washes in 100 mM cacodylate buffer (pH 7.4) prior to secondary fixation (2% osmium tetroxide) for 1 hour at room temperature. Osmium tetroxide as a secondary fixative has the advantage of preserving membrane lipids, which are not preserved using aldehyde, alone. After secondary fixation, samples were subsequently rinsed for 5 minutes in cacodylate buffer and distilled H_2O, followed

by prestaining with saturated uranyl acetate for 1 hour at room temperature. After prestaining, each sample was dehydrated with a graded ethanol series (2 × 15 minutes each: 30%, 50%, 70%, 95%; then 3 × 20 minutes each: 100%) and acetone (3 × 15 minutes) and were infiltrated with EPON epoxy resin (5 hours 30%, overnight 70%, 3 × 2-hour 40 minute 100%, 100% fresh for embed). Samples were then polymerized for 48 hours at 60°C. Ultracut was performed using Leica UC 6 ultratome with sections at 70 nm thickness and mounted on 200 mesh copper grids. The grids with the sections were stained for 20 minutes with saturated uranyl acetate and subsequently stained for 10 minutes with lead citrate. Sections were examined using a JEOL 1200EX transmission electron microscope with a Soft Imaging Systems MegaView III CCD camera.

Histochemistry

A fresh liver tissue was taken from each mouse and immediately submerged in 4% paraformaldehyde for 12 hours and 70% ethanol for 48 hours. Tissues were sectioned at 10-µm thickness, embedded in paraffin, and stained for Masson's Trichrome to assess fibrosis or hematoxylin and eosin (H&E) to determine fat droplet accumulation. Samples were imaged on Axio Scan Z.1 (Zeiss).

Native PAGE

Isolated mitochondria (100 µg) suspended in MIM were pelleted at 12,000 x g for 15 min and subsequently solubilized in 20 µL sample buffer (5 µL of 4x Native Page Sample Buffer, 8 µL 10% digitonin, 7 µL ddH_2O per sample) for 20 min on ice and then centrifuged at 20,000 x g for 30 mins at 4°C. 15 µL of the supernatant (75 µg) was collected and placed into a new tube and mixed with 2 µL of G-250 sample buffer additive. Dark blue cathode buffer (50 mLs 20X Native Page running buffer, 50 mLs 20x cathode additive, 900 mLs ddH_2O) was carefully added to the front of gel box (Invitrogen Mini Gel Tank A25977) and anode buffer (50 mLs 20x Native Page

running buffer to 950 mL ddH_2O) was carefully added to the back of the gel box making sure to not mix. The samples were then loaded onto a native PAGE 3-12% Bis-Tris Gel (BN1001BOX, Thermo Fisher Scientific), and electrophoresis was performed at 150 V for 1 hour on ice. The dark blue cathode buffer was carefully replaced with light blue cathode buffer (50 mLs 20X Native Page running buffer, 5 mL 20X cathode additive to 945 mLs ddH_2O) and run at 30 V overnight at 4°C. Gels were subsequently transferred to PVDF at 100 V, fixed with 8% acetic acid for 5 min, washed with methanol, and blotted with the following primary antibodies Anti-GRIM19 (mouse monoclonal; ab110240), Anti-SDHA (mouse monoclonal; ab14715), Anti-UQCRFS1 (mouse monoclonal; ab14746), Anti-MTCO1 (mouse monoclonal; ab14705), Anti-ATP5a (mouse monoclonal; ab14748), Anti-NDUFA9 (mouse monoclonal; ab14713) in 5% non-fat milk in TBST. Secondary anti-mouse HRP antibody listed in the key resources table and Western Lightning Plus-ECL (PerkinElmer NEL105001) was used to visualize bands.

Mitochondrial isolation

Liver tissues were minced in ice-cold mitochondrial isolation medium (MIM) buffer [300 mM sucrose, 10 mM Hepes, 1 mM EGTA, and bovine serum albumin (BSA; 1 mg/ml) (pH 7.4)] and gently homogenized with a Teflon pestle. To remove excess fat in the samples, an initial high-speed spin was performed on all samples: homogenates were centrifuged at 12,000g for 10 mins at 4°C, fat emulsion layers were removed and discarded, and resulting pellets were resuspended in MIM + BSA. Samples were then centrifuged at 800 x g for 10 min at 4°C. The supernatants were then transferred to fresh tubes and centrifuged again at 1,300 x g for 10 min at 4°C. To achieve the mitochondrial fraction (pellet), the supernatants were again transferred to new tubes and centrifuged at 12,000 x g for 10 min at 4°C. The resulting crude mitochondrial pellets were washed three times with 0.15 M KCl to remove catalase, and then spun a final time in MIM. The final mitochondrial pellets were resuspended in MIM buffer for experimental use.

Mitochondrial Respiration Measurements

Mitochondrial O_2 utilization was measured using Oroboros O2K Oxygraphs. Isolated mitochondria (50 µg for TCA substrate respiration and 100 µg for fatty acid respiration) were added to the oxygraph chambers containing assay buffer Z (MES potassium salt 105 mM, KCl 30 mM, KH_2PO_4 10 mM, $MgCl_2$ 5 mM, BSA 1 mg/ml). Respiration was measured in response to the following substrates: 0.5mM malate, 5mM pyruvate, 2.5mM ADP, 10mM succinate, 1.5 µM FCCP, 0.02mM palmitoyl-carnitine, 5mM L-carnitine.

Mitochondrial JH_2O_2

Mitochondrial H_2O_2 production was determined in isolated mitochondria from liver tissue using the Horiba Fluoromax-4/The Amplex UltraRed (10 µM)/horseradish peroxidase (3 U/ml) detection system (excitation/emission, 565:600, HORIBA Jobin Yvon Fluorolog) at 37°C. Mitochondrial protein was placed into a glass cuvette with buffer Z supplemented with 10 mM Amplex UltraRed (Invitrogen), 20 U/mL CuZn SOD). Since liver tissue is capable of producing resorufin from amplex red (AR), without the involvement of horseradish peroxidase (HRP) or H_2O_2, phenylmethylsulfonyl fluoride (PMSF) was included to the experimental medium due to its ability to inhibit HRP-independent conversion of AR to resorufin. PMSF was added to the cuvette immediately prior to measurements and at a concentration that does not interfere with biological measurements (100 µM). A 5-min background rate was obtained before adding 10 mM succinate to the cuvette to induce H_2O_2 production. After 4 min, 100 µM 1,3-bis(2-chloroethyl)-1-nitrosourea (BCNU) was added to the cuvette with 1 µM auranofin to inhibit glutathione reductase and thioredoxin reductase, respectively. After an additional 4 min, the assay was stopped, and the appearance of the fluorescent product was measured.

Site-specific electron leak was measured by systematically stimulating each site while inhibiting the other three. Site I_F was investigated in the presence of 4 mM malate, 2.5 mM ATP, 5 mM

aspartate, and 4 µM rotenone; site I_Q was measured as a 4 µM rotenone-sensitive rate in the presence of 5 mM succinate; site III_{QO} was measured as a 2 µM myxothiazol-sensitive rate in the presence of 5 mM succinate, 5 mM malonate, 4 µM rotenone, and 2 µM antimycin A; and site II_F was measured as the 1 mM malonate-sensitive rate in the presence of 0.2 mM succinate and 2 µM myxothiazol. As previously mentioned, electron leak is quantified using Amplex Red in the presence of excess superoxide dismutase, such that both superoxide and hydrogen peroxide production are accounted for by a change in fluorescence intensity (JH_2O_2) using high-resolution fluorometry (Horiba Fluoromax4®).

Phospholipidomic analysis

Liver tissue was homogenized in ice cold STEB (250 mM sucrose, 5 mM Tris-HCl, 1 mM EGTA, 0.1% fatty acid free BSA, pH 7.4, 4°C) using a tissuelyser. Mitochondria were then isolated via differential centrifugation (800 x g for 10 min, 1300 x g for 10 min, 12,000 x g for 10 min at 4°C), flushing each step under a stream nitrogen to prevent oxidation. Protein content was determined by bicinchoninic acid assay using the Pierce BCA protein assay with bovine serum albumin as a standard. To extract CoQ from mitochondria, incubations of 100 µg mitochondrial protein in 250 µL ice-cold acidified methanol, 250 µL hexane, and 1146 pmol per sample of CoQ standard (Cambridge Isotope Laboratories, CIL DLM-10279) were vortexed. The CoQ-containing hexane layer was separated by centrifugation (10 min, 17,000 x g, 4°C) and then dried down under a stream of nitrogen. Dried samples were then resuspended in methanol containing 2 mM ammonium formate and transferred to 1.5 mL glass mass spectrometry vials. Liquid chromatography-mass spectrometry (LC-MS/MS) was then performed on the reconstituted lipids using an Agilent 6530 UPLC-QTOF mass spectrometer.

Metabolomic extraction and mass spectrometry analysis

For metabolite extraction from the tissue, each sample was transferred to 2.0 mL ceramic bead mill tubes (Qiagen Catalog Number 13116-50). To each sample was added 450 µL of cold 90% methanol (MeOH) solution containing the internal standard d4-succinic acid (Sigma 293075) for every 25 mg of tissue. The samples were then homogenized in an OMNI Bead Ruptor 24. Homogenized samples were then incubated at -20 ˚C for 1 hr. After incubation the samples were centrifuged at 20,000 x g for 10 minutes at 4 ˚C. 400 µL of supernatant was then transferred from each bead mill tube into a labeled, fresh microcentrifuge tubes. Another internal standard, d27-myristic acid, was then added to each sample. Pooled quality control samples were made by removing a fraction of collected supernatant from each sample. Process blanks were made using only extraction solvent and went through the same process steps as actual samples. Everything was then dried en vacuo.

All GC-MS analysis was performed with an Agilent 5977b GC-MS MSD-HES and an Agilent 7693A automatic liquid sampler. Dried samples were suspended in 40 µL of a 40 mg/mL O-methoxylamine hydrochloride (MOX) (MP Bio #155405) in dry pyridine (EMD Millipore #PX2012-7) and incubated for one hour at 37 °C in a sand bath. 25 µL of this solution was added to auto sampler vials. 60 µL of N-methyl-N-trimethylsilyltrifluoracetamide (MSTFA with 1% TMCS, Thermo #TS48913) was added automatically via the auto sampler and incubated for 30 minutes at 37 °C. After incubation, samples were vortexed and 1 µL of the prepared sample was injected into the gas chromatograph inlet in the split mode with the inlet temperature held at 250 °C. A 10:1 split ratio was used for analysis for most metabolites. Any metabolites that saturated the instrument at the 10:1 split was analyzed at a 100:1 split ratio. The gas chromatograph had an initial temperature of 60 °C for one minute followed by a 10 °C/min ramp to 325 °C and a hold time of 10 minutes. A 30-meter Agilent Zorbax DB-5MS with 10 m Duraguard capillary column was employed for chromatographic separation. Helium was used as the carrier gas at a rate of 1 mL/min. Below is a description of the two-step derivatization

process used to convert non-volatile metabolites to a volatile form amenable to GC-MS. Pyruvic acid is used here as an example. Data were collected using MassHunter software (Agilent). Metabolites were identified and their peak area was recorded using MassHunter Quant. This data was transferred to an Excel spread sheet (Microsoft, Redmond WA). Metabolite identity was established using a combination of an in-house metabolite library developed using pure purchased standards, the NIST library and the Fiehn library. There are a few reasons a specific metabolite may not be observable through GC-MS.

Mitochondrial phospholipids enrichment

Isolated mitochondria (500 µg) from 2-month-old mice were incubated in fusion buffer [220 mM mannitol, 70 mM sucrose, 2 mM Hepes, 10 mM KH2PO4, 5 mM MgCl2, 1 mM EGTA, 10 mM glutamate, 2 mM malate, 10 mM pyruvate, and 2.5 mM ADP (pH 6.5)] for 20 min at 30°C under constant stirring agitation in the presence of 15 nmol of small unilamellar vesicles (SUVs). After fusion, mitochondria were layered on a sucrose gradient (0.6 M) and centrifuged 10 min at 10,000g at 4°C to remove SUV. Pellet was then washed in mitochondrial buffer [250 mM sucrose, 3 mM EGTA, and 10 mM tris-HCl, (pH 7.4)].

Succinate dehydrogenase assay

Liver succinate dehydrogenase activity was measured using the colorimetric SDH Detection Assay Kit (ab228560). Briefly, 10 mg liver tissue was rapidly homogenized in assay buffer, samples were centrifuged at 10,000 x g for 10 min, and supernatant transferred to a fresh tube. 20 µL of positive controls or sample was added to each well and the volume adjusted to 50 µL with SDH assay buffer. A SDH reaction mix was prepared using 46 µL SDH assay buffer, 2 µL SDH probe, and 2 µL SDH substrate mix per sample and added to each well for a final volume of 100 µL. Absorbance was measured at 600 nm at 25°C with a microplate reader in kinetic

mode. Absorbance was followed for 30 minutes and time points 10 and 30 min were selected in the linear range to calculate succinate dehydrogenase activity of the samples.

Serum AST and ALT

Mice were sacrificed by CO_2 inhalation and blood samples collected via cardiac puncture into 20 mL of heparin and centrifuged for collection of plasma within 1 hour of blood collection and frozen at -80°C until analysis. Plasma samples from mice were processed in a single batch for determination of serum alanine aminotransferase (ALT) and aspartate aminotransferase (AST) levels using a DC Element chemistry analyser (HESKA).

Quantification and statistical analyses

All data presented herein are expressed as mean ± SEM. The level of significance was set at $p < 0.05$. Student's t-tests were used to determine the significance between experimental groups and two-way ANOVA analysis followed by Tukey's HSD post hoc test was used where appropriate. The sample size (n) for each experiment is shown in the figure legends and corresponds to the sample derived from the individual mice or for cell culture experiments on an individual batch of cells. Unless otherwise stated, statistical analyses were performed using GraphPad Prism software.

Figure Legends

Figure 1. Hepatic mitochondrial phospholipidome in mouse models of MASLD

(A) H&E stains of livers from mice given standard chow or a Western HFD for 16 wks.

(B) H&E stains of livers from 20 wk old wildtype or ob/ob mice.

(C) Masson's Trichrome stains of livers from mice given standard chow or the GAN diet for 30 wks.

(D) Masson's Trichrome stains of livers from mice injected with vehicle or carbon tetrachloride for 6wks.

(E) Representative western blot of OXPHOS subunits and citrate synthase in liver tissues from mice given standard chow or a Western HFD for 16 wks (n=4 per group).

(F) Representative western blot of OXPHOS subunits and citrate synthase in liver tissues from 20 wk old wildtype or ob/ob mice (n=4 per group).

(G) Representative western blot of OXPHOS subunits and citrate synthase in liver tissues from mice given standard chow or the GAN diet for 30 wks (n=4 per group).

(H) Representative western blot of OXPHOS subunits and citrate synthase in liver tissues from mice injected with vehicle or carbon tetrachloride for 6 wks (n=4 per group).

(I) Mitochondrial phospholipidome from mice given standard chow or HFD.

(J) Mitochondrial phospholipidome from 20 wk old wildtype or ob/ob mice.

(K) Mitochondrial phospholipidome from mice given standard chow or the GAN diet for 30 wks.

(L) Mitochondrial phospholipidome from mice injected with vehicle or carbon tetrachloride for 6 wks.

(M) Venn Diagram comparing mitochondrial phospholipidome from all four models of MASLD: HFD, ob/ob, GAN, or carbon tetrachloride.

(N) CLS message for livers of mice given standard chow or a Western HFD for 16 wks.

(O) CLS message for livers from 20 wk old wildtype or ob/ob mice.

(P) CLS message for livers from mice given standard chow or the GAN diet for 30 wks.

(Q) CLS message for livers from mice injected with vehicle or carbon tetrachloride for 6 wks. Statistical significance was determined by 2-way ANOVA (I, J, K, and L) and unpaired Student's T test (N, O, P, and Q).

Figure 2. Hepatocyte-specific deletion of CLS induces MASLD/MASH

(A) A schematic for hepatocyte-specific deletion of CLS in mice.

(B) CLS mRNA abundance in livers from control and CLS-LKO mice (n=4 and 7 per group).

(C) Abundance of mitochondrial CL species in liver from control and CLS-LKO mice (n=5 and 6 per group).

(D) Body mass (n=13 and 11 per group).

(E) Body composition (n=6 and 7 per group).

(F) Liver mass (n=10 and 13 per group).

(G) H&E stains for control or CLS-LKO mice fed a chow diet, mice are 8wks old.

(H) Masson's Trichrome stains for control or CLS-LKO mice.

(I) RNA sequencing data for genes associated with MASH, liver regeneration, and HCC for control and CLS-LKO mice (n=7 and 5 per group).

(J) Serum AST from control and CLS-LKO mice (n=6 and 7 per group).

(K) Serum ALT from control and CLS-LKO mice (n=6 and 7 per group).

(L) mRNA abundance of TNFα, TGFβ, IL-12, and MCP1 in control and CLS-LKO livers (n=5 and 7 per group).

(M) Representative image of flow cell population gating for control and CLS-LKO livers (n=5 and 7 per group).

(N) Flow cytometry of cDC2 cell population in control and CLS-LKO livers (n=5 and 7 per group).

(O) Flow cytometry of F4/80+ cell population in control and CLS-LKO livers (n=5 and 7 per group).

(P) Flow cytometry of Ly6C^{hi} cell population in control and CLS-LKO livers (n=5 and 7 per group).

(Q) Flow cytometry of inflammatory monocyte cell population in control and CLS-LKO livers (n=5 and 7 per group).

(R) Flow cytometry of neutrophil cell population in control and CLS-LKO livers (n=5 and 7 per group).

(S) Flow cytometry of cDC1 cell population in control and CLS-LKO livers (n=5 and 7 per group).

Figure 3. CLS deletion increases mitochondrial respiratory capacity

(A) Glucose tolerance test (IPGTT) performed 7 days prior to sacrifice date (n=6 and 7 per group).

(B) Area under the curve for IPGTT.

(C) Pyruvate tolerance test (PTT) performed 7 days prior to sacrifice date (n=6 and 8 per group).

(D) Area under the curve for PTT.

(E) RNA sequencing pathway analysis related to lipogenesis, VLDL, and beta-oxidation for control and CLS-LKO mice (n=6 and 5 per group).

(F) mRNA levels for genes associated with components of OXPHOS.

(G) Transmission electron microscopy images of liver mitochondria from control and CLS-LKO mice (scale bars, 1 μm).

(H) Representative western blot of whole liver tissue OXPHOS subunits and citrate synthase between control and CLS-LKO mice (n=3 per group).

(I) Ratio of mitochondrial to nuclear DNA in liver tissue (n=8 per group).

(J) Representative tracing from high-resolution respirometry during TCA cycle intermediate respiration.

(K) JO_2 consumption in isolated liver mitochondria from control and CLS-LKO mice fed a chow diet in response to 0.5mM malate, 5mM pyruvate, 2.5mM ADP, 10mM succinate, and 1.5 μM FCCP (n=6 per group).

(L) JO_2 consumption in isolated liver mitochondria from control and CLS-LKO mice fed a chow diet in response to 0.02mM palmitoyl-carnitine, 5mM L-carnitine, and 2.5mM ADP (n=6 per group).

(M) Representative western blot of isolated mitochondria OXPHOS subunits between control and CLS-LKO mice (n=4 per group).

Figure 4. Stable isotope tracing with [U-^{13}C] palmitate and [U-^{13}C] glucose in hepa1-6 cells with or without CLS deletion

(A) Schematic illustration of the labeling process during stable isotope tracing with [U-^{13}C] palmitate or [U-^{13}C] glucose. Blue or green circles represent ^{13}C-labeled carbons, and red circles represent unlabeled ^{12}C carbons. The pathway shows the flow from palmitate to beta-oxidation or glucose through glycolysis to the tricarboxylic acid (TCA) cycle, with key intermediates labeled.

(B) Levels of labeled succinate from palmitate tracing in hepa1-6 cells (n=6 for shSC and shCLS).

(C) Levels of labeled malate from palmitate tracing in hepa1-6 cells (n=6 for shSC and shCLS).

(D) Levels of labeled fumarate from palmitate tracing in hepa1-6 cells (n=6 for shSC and shCLS).

(E) Levels of labeled pyruvate from glucose tracing in hepa1-6 cells (n=6 for shSC and shCLS).

(F) Levels of labeled lactic acid from glucose tracing in hepa1-6 cells (n=6 for shSC and shCLS).

(G) Levels of labeled acetyl-CoA from glucose tracing in hepa1-6 cells (n=6 for shSC and shCLS).

(H) Levels of labeled succinate from glucose tracing in hepa1-6 cells (n=6 for shSC and shCLS).

(I) Levels of labeled fumarate from glucose tracing in hepa1-6 cells (n=6 for shSC and shCLS).

(J) Levels of labeled citrate from glucose tracing in hepa1-6 cells (n=6 for shSC and shCLS).

Figure 5. CL deficiency promotes mitochondrial electron leak

(A) Electron microscopy images for control and CLS-LKO mice depicting fibrosis via red arrows. Scale bars are 2 μM.

(B) Quantitative PCR analysis of fibrotic markers (Col1a1 and Des) in liver tissue from control and CLS-LKO mice (n=5 and 7 per group).

(C) Representative image for western blot analysis of cleaved caspase-3 in liver tissue from control and CLS-LKO mice (n=4 per group).

(D) Representative image for western blot analysis of cleaved caspase-7 in liver tissue from control and CLS-LKO mice (n=4 per group).

(E) Western blot analysis and quantification of cytochrome c levels in mitochondrial fraction from liver tissue of control and CLS-LKO mice (n=7 per group).

(F) Western blot analysis and quantification of cytochrome c levels in cytosolic fraction from liver tissue of control and CLS-LKO mice (n=7 per group).

(G) H_2O_2 emission and production in isolated liver mitochondria from control and CLS-LKO mice fed a chow diet, stimulated with succinate, or succinate, auranofin, and BCNU (n=3 and 4 per group).

(H) Schematic representation of rescue experiment. Isolated mitochondria from CLS-LKO mice were enriched with small unilamellar vesicles (SUVs) containing either cardiolipin (CL) or phosphatidylcholine (PC).

(I) Quantification of H_2O_2 production in liver mitochondria enriched with CL or PC SUVs in control and CLS-LKO mice (n=4 per group).

Figure 6. Influence of CL deficiency on site-specific electron leak and supercomplex formation

(A) Electron leak at site I_Q in mitochondria from control and CLS-LKO mice (n=7 per group).

(B) Electron leak at site I_F in mitochondria from control and CLS-LKO mice (n=7 per group.

(C) Electron leak at site II_F in mitochondria from control or CLS-LKO mice (n=7 per group).

(D) Electron leak at site III_{Q0} in mitochondria from control or CLS-LKO mice (n=7 per group).

(E) Abundance of respiratory supercomplex I formation using the GRIM19 antibody in isolated mitochondria from livers taken from control and CLS-LKO mice (n=4 per group).

(F) Quantification of E.

(G) Abundance of respiratory supercomplex I formation using the NDUFA9 antibody in isolated mitochondria from livers taken from control and CLS-LKO livers (n=4 per group).

(H) Quantification of G.

(I) Abundance of respiratory supercomplex II formation using the SDHA2 antibody in isolated mitochondria from livers taken from control and CLS LKO livers (n=4 per group).

(J) Quantification of I.

(K) Abundance of respiratory supercomplex III formation using the UQCRFS1 antibody in isolated mitochondria from livers taken from control and CLS-LKO livers (n=4 per group).

(L) Quantification of K.

(M) Abundance of respiratory supercomplex IV formation using the MTCO1 antibody in isolated mitochondria from livers taken from control and CLS-LKO livers (n=4 per group).

(N) Quantification of M.

(O) Abundance of respiratory supercomplex V formation using the ATP5A antibody in isolated mitochondria from livers taken from control and CLS-LKO livers (n=4 per group).

(P) Quantification of O.

Figure 7. CL deficiency disrupts coenzyme Q homeostasis in mice and humans

(A) Chemical structure of Coenzyme Q (CoQ) in its oxidized (ubiquinone) and reduced (ubiquinol) forms.

(B) Oxidized CoQ levels in isolated mitochondrial fractions from livers taken from control and CLS-LKO mice (n=7 per group).

(C) Reduced CoQ levels in isolated mitochondrial fractions from livers taken from control and CLS-LKO livers (n=7 per group).

(D) Succinate-to-fumarate ratio from untargeted metabolomics showing differential abundance of TCA cycle metabolites in livers taken from CLS-LKO mice compared to controls (n=5 and 7 per group).

(E) Activity of succinate dehydrogenase (SDH) in control and CLS-LKO livers (n=6 per group).

(F) Representative histological images using H&E stain on human liver samples from patients with advanced steatohepatitis.

(G) Analysis of CL in human liver samples from patients with advanced steatohepatitis (n=10 and 16 per group).

(H) Analysis of CoQ in human liver samples from patients with advanced steatohepatitis (n=10 and 16 per group).

(I) Pearson correlation analysis of CL and CoQ levels in human liver samples ($R^2 = 0.64$).

References

1. Younossi, Z.M., *et al.* Global epidemiology of nonalcoholic fatty liver disease—Meta-analytic assessment of prevalence, incidence, and outcomes. *Hepatology* **64**, 73-84 (2015).
2. Miao, L.T., Giovanni; Byrne, Christopher D; Cao, Ying-Ying; Zheng, Ming-Hua. Current status and future trends of the global burden of MASLD. *Trends in Endocrinology & Metabolism* **29**, 1043-2760 (2024).
3. Saito, K., *et al.* Characterization of hepatic lipid profiles in a mouse model with nonalcoholic seatohepatitis and subsequent fibrosis. **5**(2015).
4. John, B.S.S. Nonalcoholic Steatohepatitis (NASH). in *StatPearls* (StatPearls Publishing, Treasure Island, 2023).
5. Vigano, L., Lleo, A. & Aghemo, A. Non-alcoholic fatty liver disease, non-alcoholic steatohepatitis, metabolic syndrome and hepatocellular carcinoma—a composite scenario. *Hepatobiliary Surgery and Nutrition* **7**, 130-133 (2018).
6. Fan, J.-G. & Cao, H.-X. Role of diet and nutritional management in non-alcoholic fatty liver disease. *Gastroenterology and Hepatology* **28**, 87-87 (2013).
7. Gordon, D.L., *et al.* Biomarkers of NAFLD progression: a lipidomics approach to an epidemic. *Journal of Lipid Research* **56**, 722-736 (2015).
8. Fu, S., *et al.* Aberrant lipid metabolism disrupts calcium homeostasis causing liver endoplasmic reticulum stress in obesity. *Nature* **473**, 528-531 (2011).
9. Simoes, I.C.M., Fontes, A., Pinton, P., Zischka, H. & Wieckowski, M.R. Mitochondria in non-alcoholic fatty liver disease. *The International Journal of Biochemistry & Cell Biology* **95**, 93-99 (2018).
10. Leveille, M. & Estall, J.L. Mitochondrial Dysfunction in the Transition from NASH to HCC. *Metabolites* **9**, 233 (2019).
11. Einer, C., *et al.* Mitochondrial adaptation in steatotic mice. **59**, 483-495 (2018).
12. Sunny, N.E., Bril, F. & Cusi, K. Mitochondrial Adaptation in Nonalcoholic Fatty Liver Disease: Novel Mechanisms and Treatment Strategies. **28**(2018).
13. Noureddin, M. & Sanyal, A.J. Pathogenesis of NASH: the Impact of Multiple Pathways. **17**, 350-360 (2018).
14. Pfeiffer, K., *et al.* Cardiolipin stabilizes respiratory chain supercomplexes. **278**, 52873-52880 (2003).
15. Johnson, J.M., *et al.* Targeted overexpression of catalase to mitochondria does not prevent cardioskeletal myopathy in Barth syndrome. **121**, 94-102 (2018).
16. Houtkooper, R.H. & Vaz, F.M. Cardiolipin, the heart of mitochondrial metabolism. *Cell. Mol. Life Sci.* **65**, 2493-2506 (2008).
17. Schlame ab, M. & Hostetler, K.Y. Cardiolipin synthase from mammalian mitochondria. *Biochimica et Biophysica Acta (BBA) - Molecular and Cell Biology of Lipids* **1348**, 207-213 (1997).
18. Paradies, G., Paradies, V., Ruggiero, F.M. & Petrosillo, G. Role of Cardiolipin in Mitochondrial Function and Dynamics in Health and Disease: Molecular and Pharmacological Aspects. *Cells* **8**, 728 (2019).
19. Funai, K., Summers, S.A. & Rutter, J. Reign in the membrane: How common lipids govern mitochondrial function. *Current opinion in cell biology* **63**, 162-173 (2020).
20. Jussupow, A., Luca, A.D. & Kaila, V.R. How cardiolipin modulates the dynamics of respiratory complex I. *Science Advances* **5**(2019).
21. Schwall, C.T., Greenwood, V.L. & Alder, N.N. The stability and activity of respiratory Complex II is cardiolipin-dependent. *Biochimica et Biophysica Acta (BBA) - Molecular and Cell Biology of Lipids* **1817**, 1588-1596 (2012).

22. Bazan, S.*, et al.* Cardiolipin-dependent Reconstitution of Respiratory Supercomplexes from Purified Saccharomyces cerevisiae Complexes III and IV*. **288**, 401-411 (2013).
23. Dudek, J.*, et al.* Cardiolipin deficiency affects respiratory chain function and organization in an induced pluripotent stem cell model of Barth syndrome. *Stem Cell Research* **11**, 806-819 (2013).
24. Sustarsic, E.G.*, et al.* Cardiolipin Synthesis in Brown and Beige Fat Mitochondria Is Essential for Systemic Energy Homeostasis. *Cell Metabolism* **28**, 159-174 (2018).
25. Jiang, F.*, et al.* Absence of cardiolipin in the crd1 null mutant results in decreased mitochondrial membrane potential and reduced mitochondrial function. **275**, 22387-22394 (2000).
26. Xu, Y., Sutachan, J.J., Plesken, H., Kelley, R.I. & Schlame, M. Characterization of lymphoblast mitochondria from patients with Barth syndrome. **85**, 823-830 (2005).
27. Hsu, P.*, et al.* Cardiolipin remodeling by TAZ/tafazzin is selectively required for the initiation of mitophagy. *Autophagy* **11**, 643-652 (2015).
28. Le, C.H.*, et al.* Tafazzin deficiency impairs CoA-dependent oxidative metabolism in cardiac mitochondria. *Journal of Biological Chemistry* **295**, 12485-12497 (2020).
29. Heden, T.D.*, et al.* Mitochondrial PE potentiates respiratory enzymes to amplify skeletal muscle aerobic capacity. *Science Advances* **5**, 8352 (2019).
30. Johnson, J.M.P., Alek D; Balderas, Enrique; Sustarsic, Elahu G; Maschek, J Alan; Brothwell, Marisa J; Alejandro, Jara-Ramos; Panic, Vanja; Morgan, Jeffrey T; Villanueva, Claudio J; Sanchez, Alejandro; Rutter, Jared; Lodhi, Irfan J; Cox, James E; Fisher-Wellman, Kelsey H; Chaudhuri, Dipayan; Gerhart-Hines, Zachary; Funai, Katsuhiko. Mitochondrial phosphatidylethanolamine modulates UCP1 to promote brown adipose thermogenesis. *Science Advances* **9**, 7864 (2023).
31. Kartsoli, S., Kostara, C.E., Tsimihodimos, V., Bbairaktari, E.T. & Christodoulou, D.K. Lipidomics in non-alcoholic fatty liver disease. *World Journal of Hepatology* **12**, 436-450 (2020).
32. Ehud Zigmond, C.V. Two Roads Diverge in the Sick Liver, Monocytes Travel Both. *Cell Press* **10**, 1016 (2020).
33. Zahao, X.-A.C., Guang-Mei; Liu, Yong; Chen, Yu-Xin; Wu, Hong-Yan; Chen, Jin; Xiong, Ya-Li; Tian, Chen; Wang, Gui-Yang; Jia, Bei; Xia, Juan; Wang, Jian; Yan, Xiao-Min; Zhang, Zhao-Ping; Huang, Rui; Wu, Chao. Inhibitory effect of silymarin on CCl4-induced liver fibrosis by reducing Ly6Chi monocytes infiltration. *International Journal of Clinical & Experimental Pathology* **10**, 11941-11951 (2017).
34. Daemen, S.G., Anastasiia; Kalugotla, Gowri; He, Li; Chan, Mandy M.; Beals, Joseph W.: Liss, Kim H.; Klein, Samuel; Feldstein, Ariel E.; Finck, Brian N.; Artyomov, Maxim N.; Schilling, Joel D. Dynamic Shifts in the Composition of Resident and Recruited Macrophages Influence Tissue Remodeling in NASH. *Cell Reports* **34**, 108626 (2021).
35. Liyanage, S.E.G., Peter J.; Ribeiro, Joana; Cristante, Enrico; Sampson, Robert D.; Luhmann, Ulrich F.O.; Ali, Robin R.; Bainbridge, James W. Flow cytometric analysis of inflammatory and resident myeloid populations in mouse ocular inflammatory models. *Experimental Eye Research* **151**, 160-170 (2016).
36. Fry, M. & Green, D.E. Cardiolipin requirement for electron transfer in complex I and III of the mitochondrial respiratory chain. *J. Biol Chem* **256**, 1874-1880 (1981).
37. Paradies, G., Petrosillo, G., Pistolese, M. & Ruggiero, F.M. Reactive oxygen species affect mitochondrial electron transport complex I activity through oxidative cardiolipin damage. *Gene* **286**, 135-141 (2002).
38. Lange, C., Nett, J.H., Trumpower, B.L. & Hunte, C. Specific roles of protein–phospholipid interactions in the yeast cytochrome bc1 complex structure. *EMBO J* **20**, 6591-6600 (2001).

39. Robinson, N.C. Functional binding of cardiolipin to cytochrome c oxidase. *J Bioenerg Biomembr* **25**, 153-163 (1993).
40. Koliaki, C.*, et al.* Adaptation of hepatic mitochondrial function in humans with non-alcoholic fatty liver is lost in steatohepatitis. *Cell Metabolism* **21**, 739-746 (2015).
41. Siripoksup, P.*, et al.* Sedentary behavior in mice induces metabolic inflexibility by suppressing skeletal muscle pyruvate metabolism. *J Clin Invest* **134**(2024).
42. Drose, S. & Brandt, U. The Mechanism of Mitochondrial Superoxide Production by the Cytochrome bc1 Complex. *Journal of Biological Chemistry* **283**, 21649-21654 (2008).
43. Marra, F. & Svegliati-Baroni, G. Lipotoxicity and the gut-liver axis in NASH pathogenesis. *Hepatology* **68**, 280-295 (2018).
44. Buzzetti, E., Pinzani, M. & Tsochatzis, E.A. The multiple-hit pathogenesis of non-alcoholic fatty liver disease (NAFLD). **65**, 1038-1048 (2016).
45. Turkseven, S.*, et al.* Mitochondria-targeted antioxidant mitoquinone attenuates liver inflammation and fibrosis in cirrhotic rats. *American Physiological Society* **318**, 298-304 (2020).
46. Karakuzu, O.C., Melissa R.; Liu, Yi; Garsin, Danielle A. Amplex Red Assay for Measuring Hydrogen Peroxide Production from Caenorhabditis elegans. *Bio Protec.* **9**, 3409 (2019).
47. Prola, A.B., Jordan; Vandestienne, Aymeline; Piquereau, Jerome; Denis, Raphael GP; Guyot, Stephane; Chauvin, Hadrien; Mourier, Arnaud; Maurer, Marie; Henry, Celine; Khadhraoui, Nahed; Gallerne, Cindy; Molinie, Thibaut; Courtin, Guillaume; Gressette, Melanie; Solgadi, Audrey; Dumont, Florent; Castel, Julien; Ternacle, Julien; Demarquoy, Jean; Malgoyre, Alexandra; Koulmann, Nathalie; Derumeaux, Genevieve; Giraud, Marie-France; Joubert, Frederic; Veksler, Vladimir; Luquet, Serve; Relaix, Frederic; Tiret, Laurent; Pilot-Storck, Fanny. Cardiolipin content controls mitochondrial coupling and energetic efficiency in muscle. *Science Advances* **7**(2021).
48. Pennington, E.R., Funai, K., Brown, D.A. & Shaikh, S.R. The role of cardiolipin concentration and acyl chain composition on mitochondrial inner membrane molecular organization and function. *Biochimica et Biophysica Acta (BBA) - Molecular and Cell Biology of Lipids* **1864**, 1039-1052 (2019).
49. Mileykovskaya, E. & Dowhan, W. Cardiolipin-Dependent Formation of Mitochondrial Respiratory Supercomplexes. *Chemistry and Physics of Lipids* **179**, 42-48 (2014).
50. Arnarez, C., Marrink, S.J. & Periole, X. Molecular mechanism of cardiolipin-mediated assembly of respiratory chain supercomplexes. *Chemical Science* (2016).
51. Bottinger, L.*, et al.* Phosphatidylethanolamine and Cardiolipin Differentially Affect the Stability of Mitochondrial Respiratory Chain Supercomplexes. **5**, 677-686 (2012).
52. Dornas, W. & Schuppan, D. Mitochondrial oxidative injury: a key player in nonalcoholic fatty liver disease. *Gastrointestinal and Liver Physiology* **319**, G400-G411 (2020).
53. Gomez, B. & Robinson, N.C. Quantitative Determination of Cardiolipin in Mitochondrial Electron Transferring Complexes by Silicic Acid High-Performance Liquid Chromatography. *Analytical Biochemistry* **267**, 212-216 (1999).
54. Brand, M.D. Mitochondrial generation of superoxide and hydrogen peroxide as the source of mitochondrial redox signaling. *Free Radical Biology and Medicine* **100**, 14-31 (2016).
55. Decker, S.T.F., Katsuhiko. Mitochondrial membrane lipids in the regulation of bioenergetic flux. *Cell Metabolism* **36**, 1963-1978 (2024).
56. Bessone, F., Razori, M.V. & Roma, M.G. Molecular pathways of nonalcoholic fatty liver disease development and progression. **76**, 99-128 (2019).
57. Ines C. M. Simoes, R.A., Jose Teixeira, Agnieszka Karkucinska-Wieckowska, Adriana Carvalho, Susana P. Pereira, Rui F. Simoes, Sylwia Szymanska, Michal Dabrowski, Justyna Janikiewicz, Agnieszka Dobrzyn, Paulo J. Oliveira, Yaiza Potes, Mariusz R.

Wieckowski. The Alterations of Mitochondrial Function during NAFLD Progression-- An Independent Effect of Mitochondrial ROS Production. *International Journal of Molecular Sciences* **22**, 6848 (2021).

58. Simoes, I.C., Fontes, A., Pinton, P., Zischka, H. & Wieckowski, M.R. Mitochondria in non-alcoholic fatty liver disease. **95**, 93-99 (2017).

59. Goncalves, R.L.S., Schlame, M., Bartelt, A.L., Brand, M.D. & Hotamisligil, G.S. Cardiolipin deficiency in Barth syndrome is not associated with increased superoxide/H2O2 production in heart and skeletal muscle mitochondria. **595**, 415-432 (2021).

60. Xu, Y.*, et al.* Loss of protein association causes cardiolipin degradation in Barth syndrome. *Nature Chemical Biology* **12**, 641-647 (2016).

61. Simoes, I.C.A., Ricardo; Teixeira, Jose; Karkucinska-Wieckowska, Agnieszka; Carvalho, Adriana; Pereira, Susana P.; Simoes, Rui F.; Szymanska Sylwia; Dabrowski, Michal; Janikiewicz, Justyna; Dobrzyn, Agnieszka; Oliveira, Paulo J.; Potes, Yaiza; Wieckowski, Mariusz R. . The Alterations of Mitochondrial Function during NAFLD Progression-- An Independent Effect of Mitochondrial ROS Production. *Int J Mol Sci* **22**, 6848 (2021).

Graphical Abstract

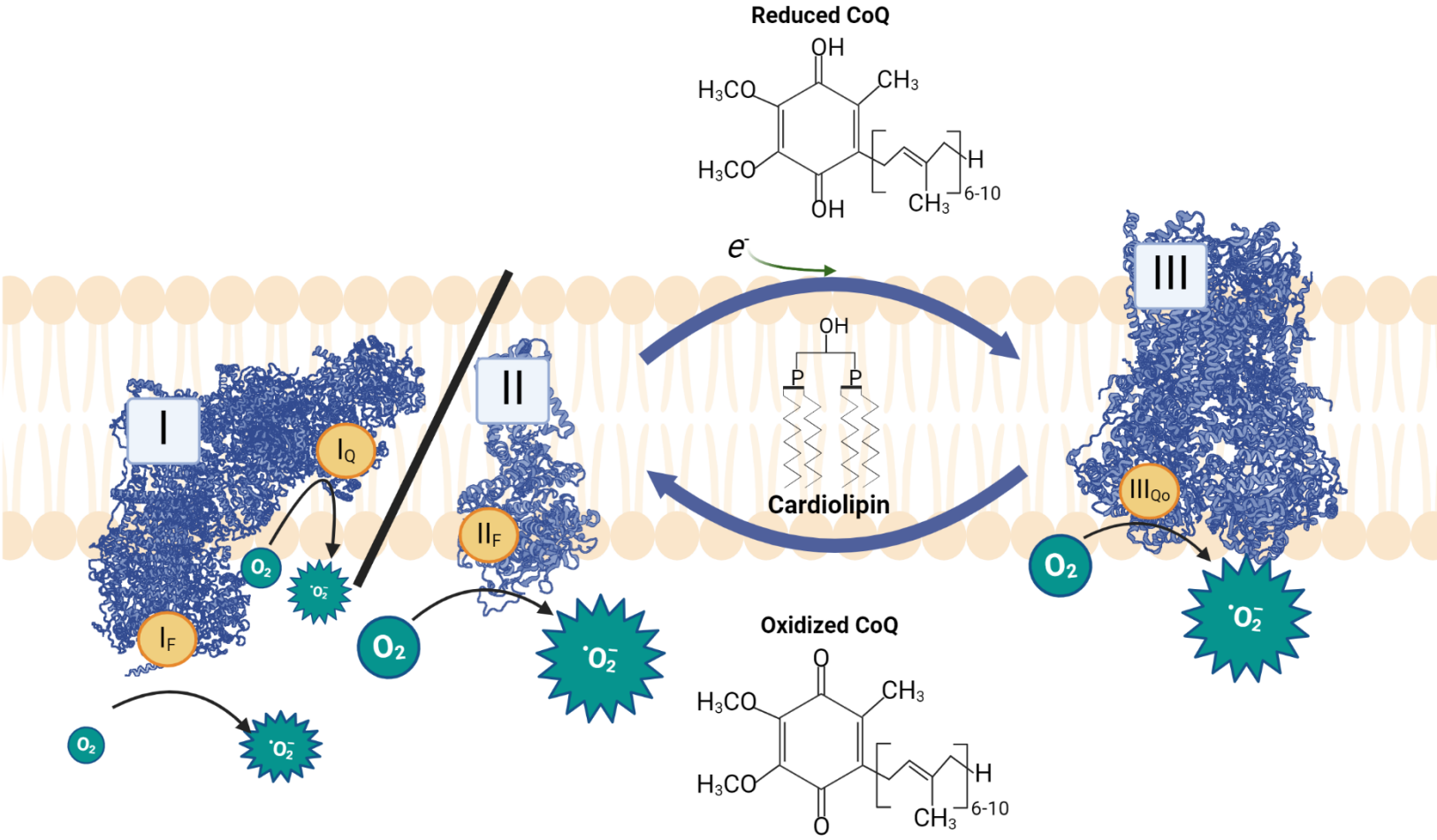

Figure 1

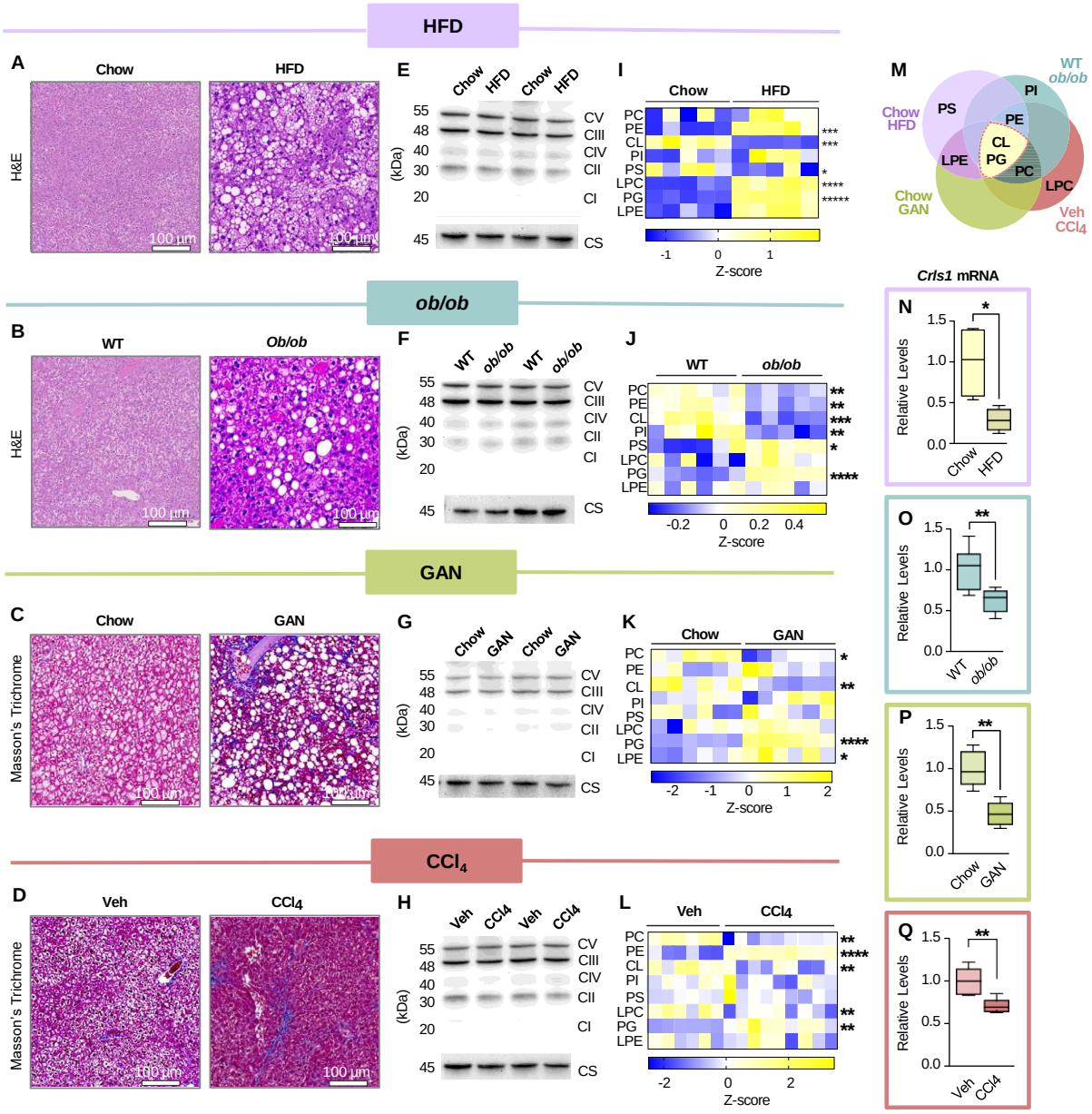
HFD
ob/ob
GAN
CCl4
A
Chow
HFD
H&E
100 µm
B
WT
Ob/ob
C
Chow
GAN
Masson's Trichrome
D
Veh
CCl4
E
F
G
H
(kDa)
CV
CIII
CIV
CII
CI
CS
I
J
K
L
Z-score
M
WT
ob/ob
Chow
HFD
Chow
GAN
Veh
CCl4
PS
PI
PE
CL
PG
PC
LPE
LPC
Crls1 mRNA
N
O
P
Q
Relative Levels

Figure 2

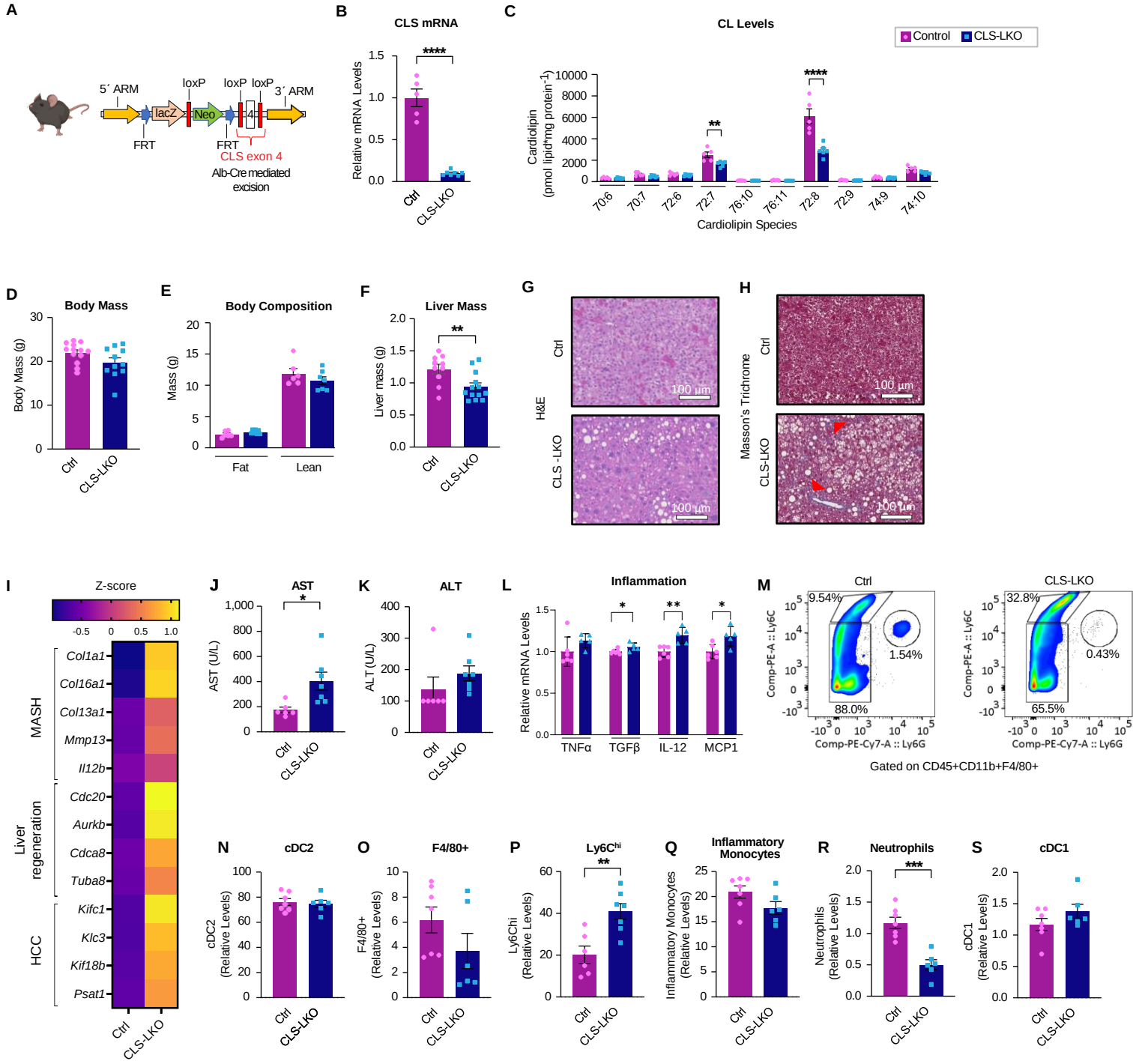
A
5´ ARM
lacZ
loxP
Neo
loxP
loxP
3´ ARM
FRT
FRT
CLS exon 4
Alb-Cre mediated excision
B
CLS mRNA
Relative mRNA Levels
Ctrl
CLS-LKO
C
CL Levels
Control
CLS-LKO
Cardiolipin (pmol lipid*mg protein-1)
Cardiolipin Species
D
Body Mass
Body Mass (g)
E
Body Composition
Mass (g)
Fat
Lean
F
Liver Mass
Liver mass (g)
G
H&E
Ctrl
CLS -LKO
100 µm
H
Masson's Trichrome
Ctrl
CLS-LKO
I
Z-score
MASH
Liver regeneration
HCC
Col1a1
Col16a1
Col13a1
Mmp13
Il12b
Cdc20
Aurkb
Cdca8
Tuba8
Kifc1
Klc3
Kif18b
Psat1
J
AST
AST (U/L)
K
ALT
ALT (U/L)
L
Inflammation
Relative mRNA Levels
TNFα
TGFβ
IL-12
MCP1
M
Ctrl
CLS-LKO
9.54%
1.54%
88.0%
32.8%
0.43%
65.5%
Comp-PE-A :: Ly6C
Comp-PE-Cy7-A :: Ly6G
Gated on CD45+CD11b+F4/80+
N
cDC2
cDC2 (Relative Levels)
O
F4/80+
F4/80+ (Relative Levels)
P
Ly6Chi
Ly6Chi (Relative Levels)
Q
Inflammatory Monocytes
Inflammatory Monocytes (Relative Levels)
R
Neutrophils
Neutrophils (Relative Levels)
S
cDC1
cDC1 (Relative Levels)

Figure 3

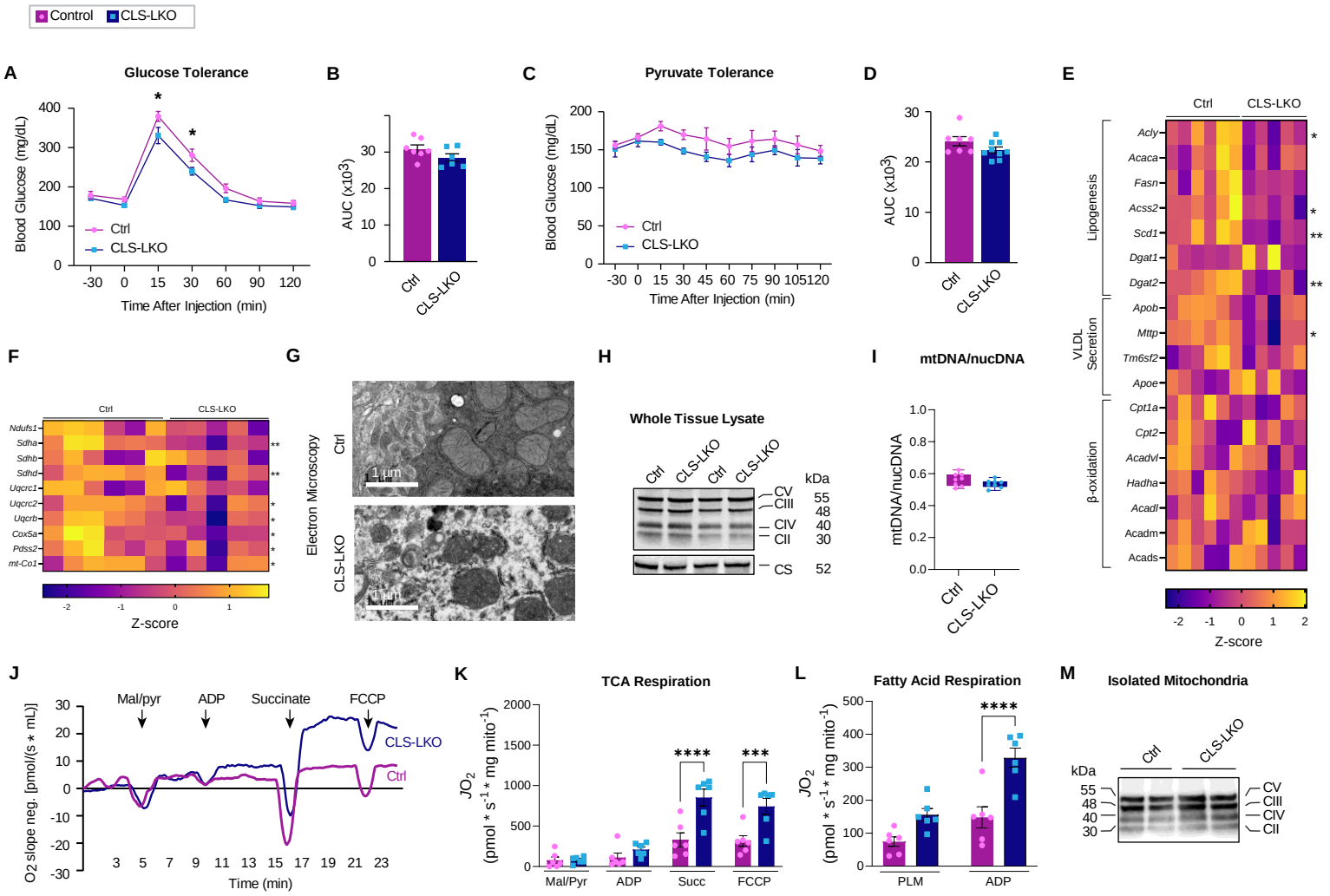
Control
CLS-LKO
A
Glucose Tolerance
Blood Glucose (mg/dL)
Time After Injection (min)
Ctrl
CLS-LKO
B
AUC (x10^3)
C
Pyruvate Tolerance
D
E
Lipogenesis
VLDL Secretion
β-oxidation
Acly
Acaca
Fasn
Acss2
Scd1
Dgat1
Dgat2
Apob
Mttp
Tm6sf2
Apoe
Cpt1a
Cpt2
Acadvl
Hadha
Acadl
Acadm
Acads
Z-score
F
Ndufs1
Sdha
Sdhb
Sdhd
Uqcrc1
Uqcrc2
Uqcrb
Cox5a
Pdss2
mt-Co1
G
Electron Microscopy
1 µm
H
Whole Tissue Lysate
kDa
CV
CIII
CIV
CII
CS
I
mtDNA/nucDNA
J
Mal/pyr
ADP
Succinate
FCCP
O2 slope neg. [pmol/(s * mL)]
Time (min)
K
TCA Respiration
JO2 (pmol * s-1 * mg mito-1)
Mal/Pyr
Succ
L
Fatty Acid Respiration
PLM
M
Isolated Mitochondria

Figure 4

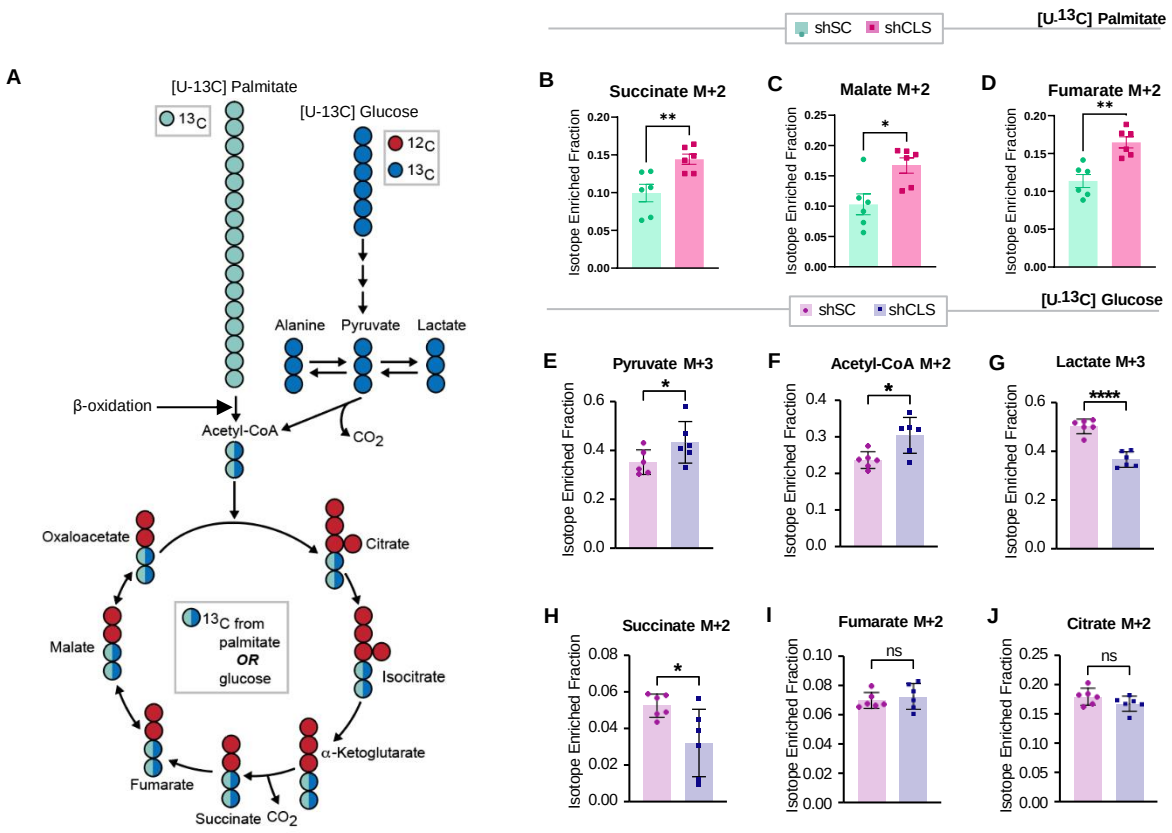
A
[U-13C] Palmitate
13C
[U-13C] Glucose
12C
13C
Alanine
Pyruvate
Lactate
β-oxidation
Acetyl-CoA
CO2
Oxaloacetate
Citrate
Malate
13C from palmitate OR glucose
Isocitrate
α-Ketoglutarate
Fumarate
Succinate
CO2
shSC
shCLS
[U-13C] Palmitate
B
Succinate M+2
C
Malate M+2
D
Fumarate M+2
Isotope Enriched Fraction
shSC
shCLS
[U-13C] Glucose
E
Pyruvate M+3
F
Acetyl-CoA M+2
G
Lactate M+3
H
Succinate M+2
I
Fumarate M+2
J
Citrate M+2
ns

Figure 5

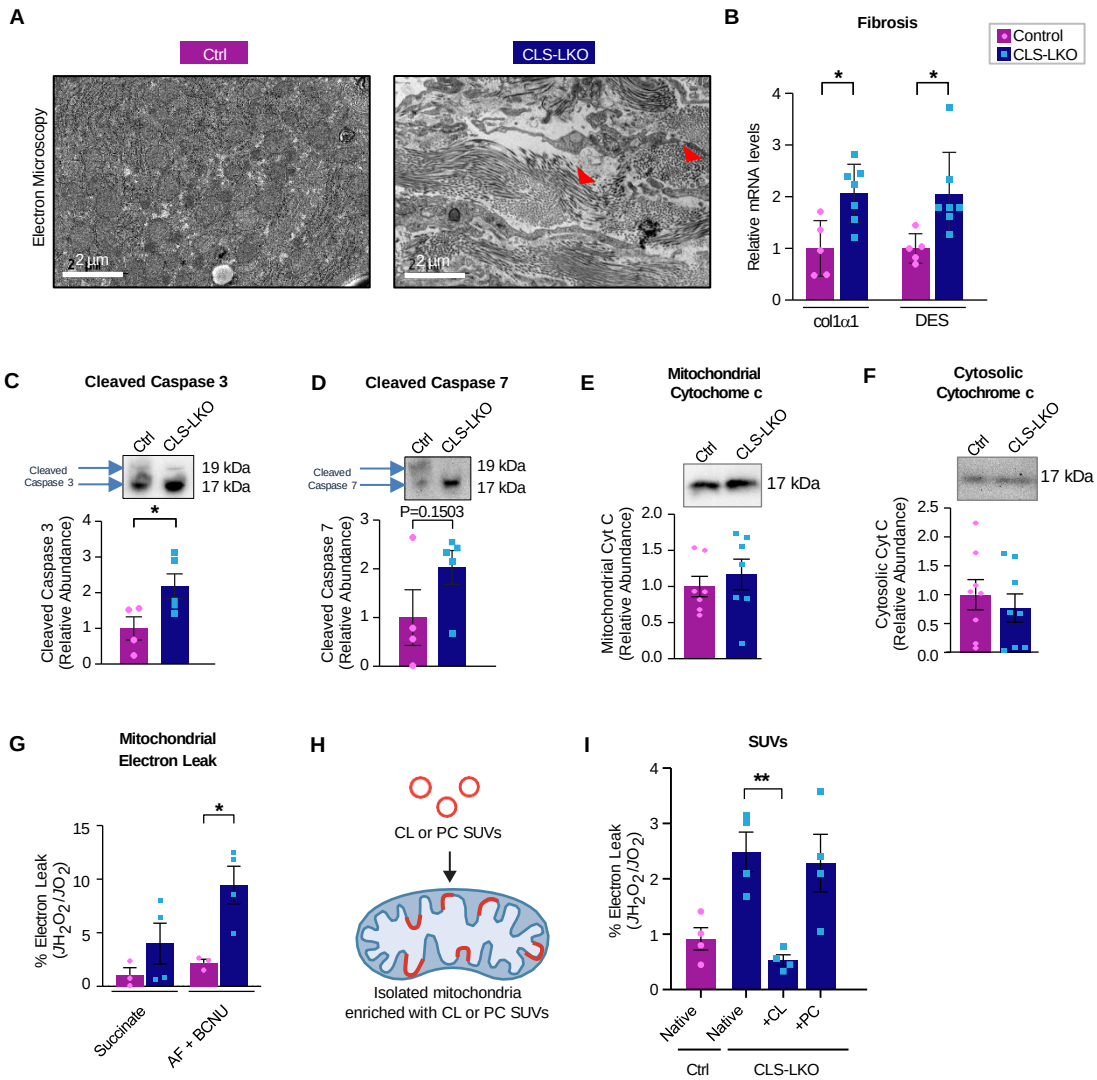
A
Ctrl
CLS-LKO
Electron Microscopy
2 µm
2 µm
B
Fibrosis
Control
CLS-LKO
Relative mRNA levels
col1α1
DES
C
Cleaved Caspase 3
Ctrl
CLS-LKO
Cleaved Caspase 3
19 kDa
17 kDa
Cleaved Caspase 3 (Relative Abundance)
D
Cleaved Caspase 7
Cleaved Caspase 7
P=0.1503
Cleaved Caspase 7 (Relative Abundance)
E
Mitochondrial Cytochome c
17 kDa
Mitochondrial Cyt C (Relative Abundance)
F
Cytosolic Cytochrome c
17 kDa
Cytosolic Cyt C (Relative Abundance)
G
Mitochondrial Electron Leak
% Electron Leak (JH_2O_2/JO_2)
Succinate
AF + BCNU
H
CL or PC SUVs
Isolated mitochondria enriched with CL or PC SUVs
I
SUVs
% Electron Leak (JH_2O_2/JO_2)
Native
Native
+CL
+PC
Ctrl
CLS-LKO

Figure 6

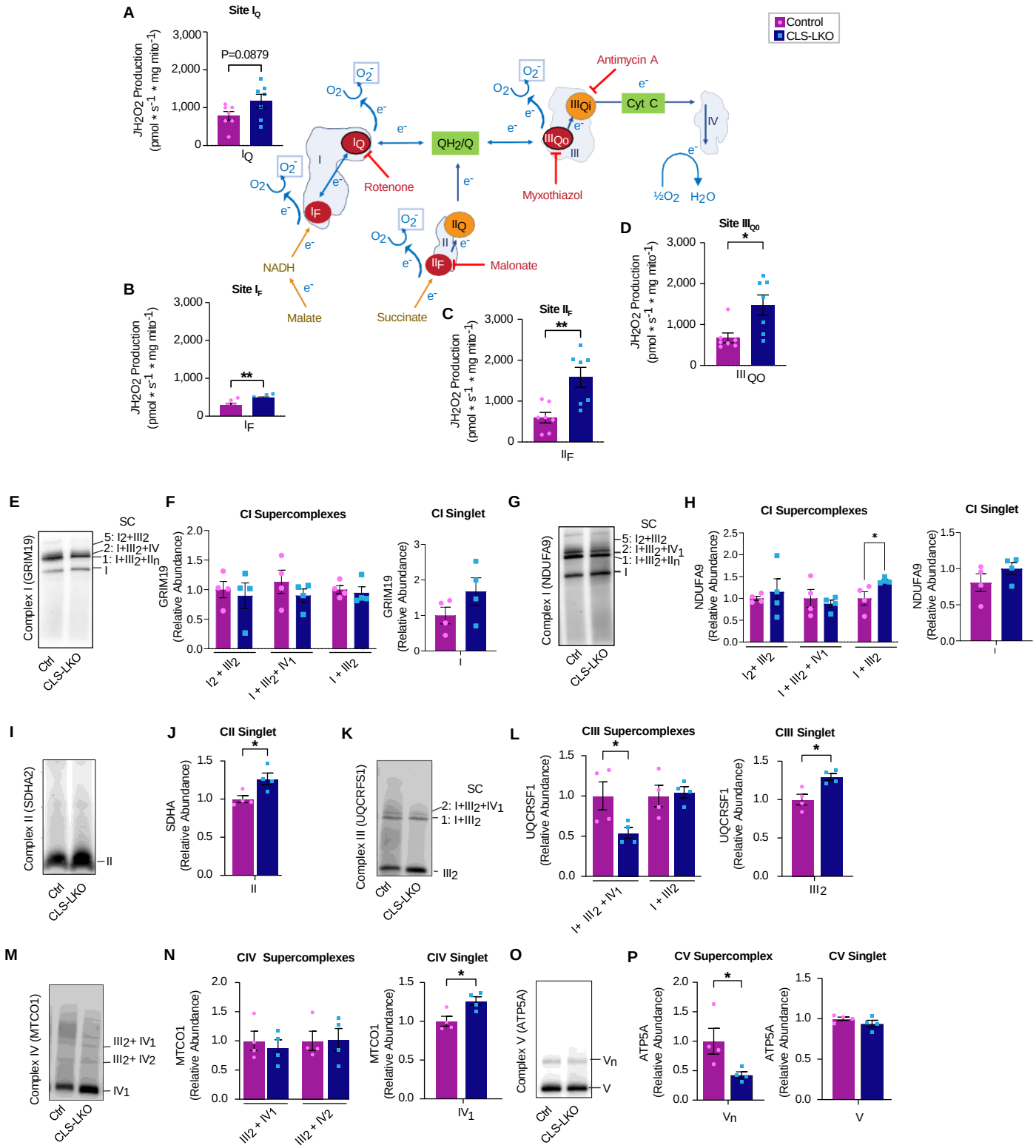
A
Site I_Q
P=0.0879
JH_2O_2 Production (pmol * s^{-1} * mg mito^{-1})
Control
CLS-LKO
Antimycin A
Cyt C
Rotenone
Myxothiazol
Malonate
NADH
Malate
Succinate
½O2 H2O
B
Site I_F
C
Site II_F
D
Site III_{Qo}
E
SC
Complex I (GRIM19)
Ctrl
CLS-LKO
F
CI Supercomplexes
CI Singlet
GRIM19 (Relative Abundance)
G
Complex I (NDUFA9)
H
NDUFA9 (Relative Abundance)
I
Complex II (SDHA2)
J
CII Singlet
SDHA (Relative Abundance)
K
Complex III (UQCRFS1)
L
CIII Supercomplexes
CIII Singlet
UQCRSF1 (Relative Abundance)
M
Complex IV (MTCO1)
N
CIV Supercomplexes
CIV Singlet
MTCO1 (Relative Abundance)
O
Complex V (ATP5A)
P
CV Supercomplex
CV Singlet
ATP5A (Relative Abundance)

Figure 7

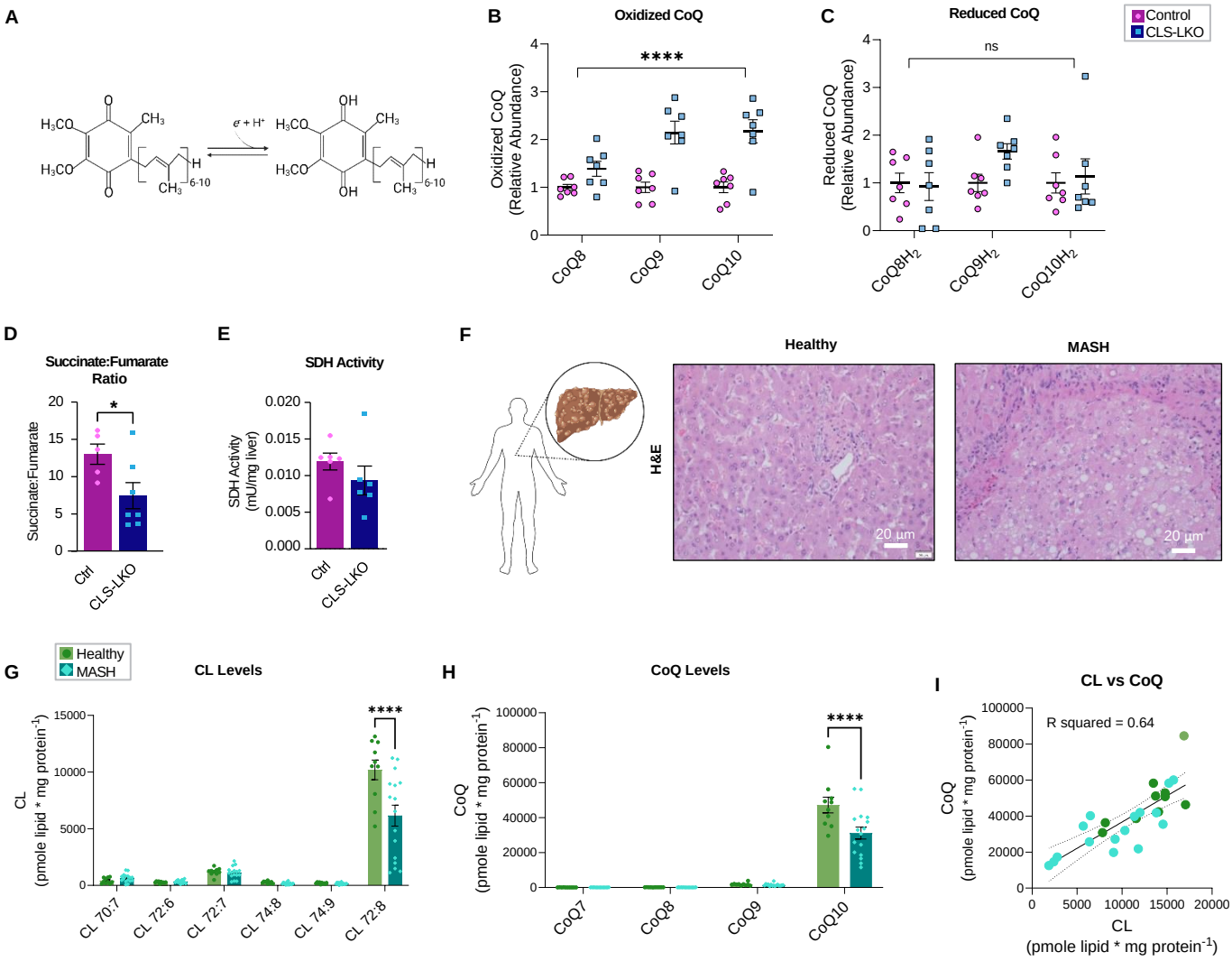
A
B
Oxidized CoQ
Oxidized CoQ (Relative Abundance)
****
CoQ8
CoQ9
CoQ10
C
Reduced CoQ
Reduced CoQ (Relative Abundance)
ns
Control
CLS-LKO
CoQ8H2
CoQ9H2
CoQ10H2
D
Succinate:Fumarate Ratio
Succinate:Fumarate
*
Ctrl
CLS-LKO
E
SDH Activity
SDH Activity (mU/mg liver)
F
Healthy
MASH
H&E
20 µm
G
Healthy
MASH
CL Levels
CL (pmole lipid * mg protein-1)
CL 70:7
CL 72:6
CL 72:7
CL 74:8
CL 74:9
CL 72:8
H
CoQ Levels
CoQ (pmole lipid * mg protein-1)
CoQ7
CoQ8
CoQ9
CoQ10
I
CL vs CoQ
R squared = 0.64
CoQ (pmole lipid * mg protein-1)
CL (pmole lipid * mg protein-1)

Supplemental Figure S1

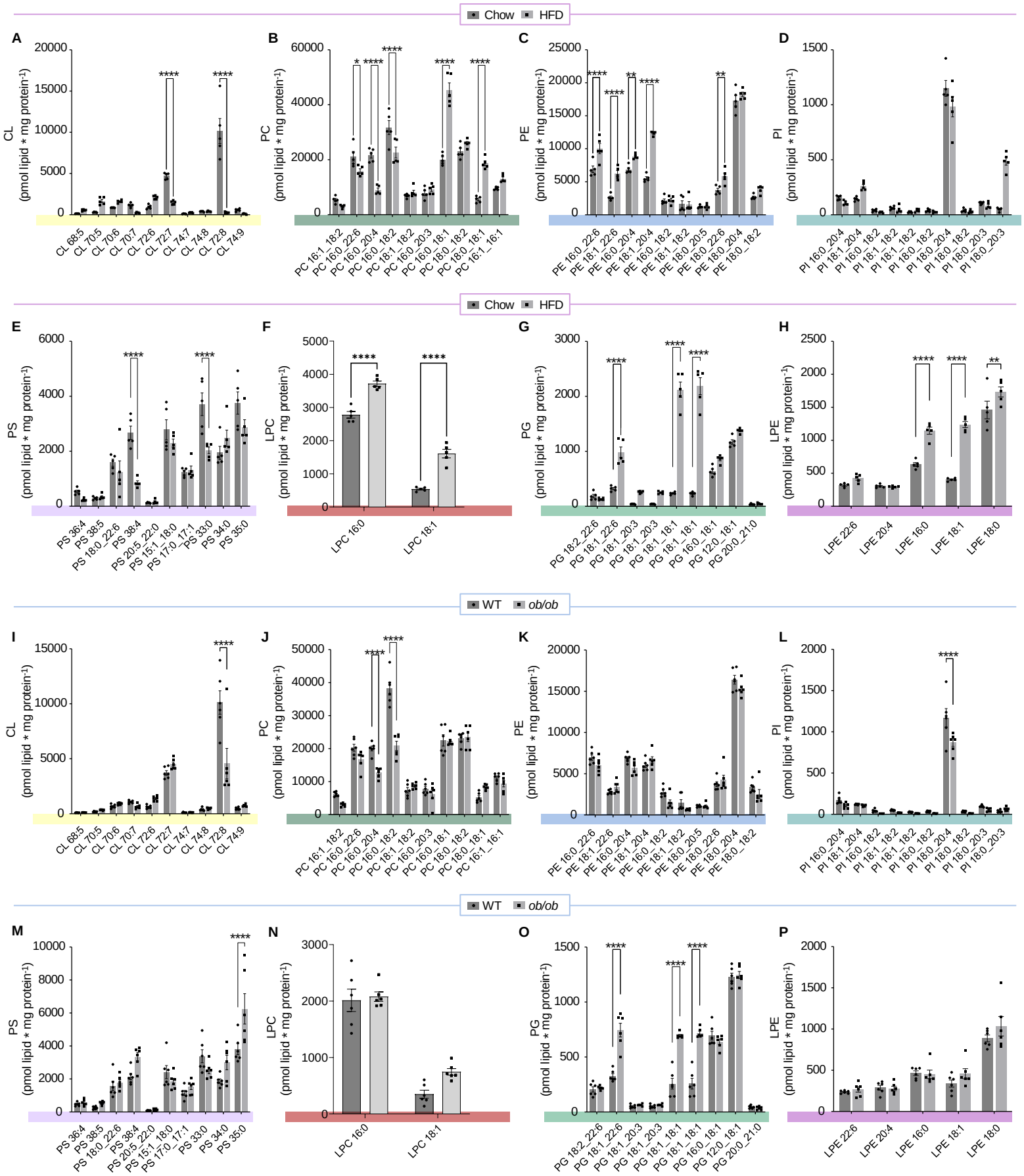

Supplemental Figure S2

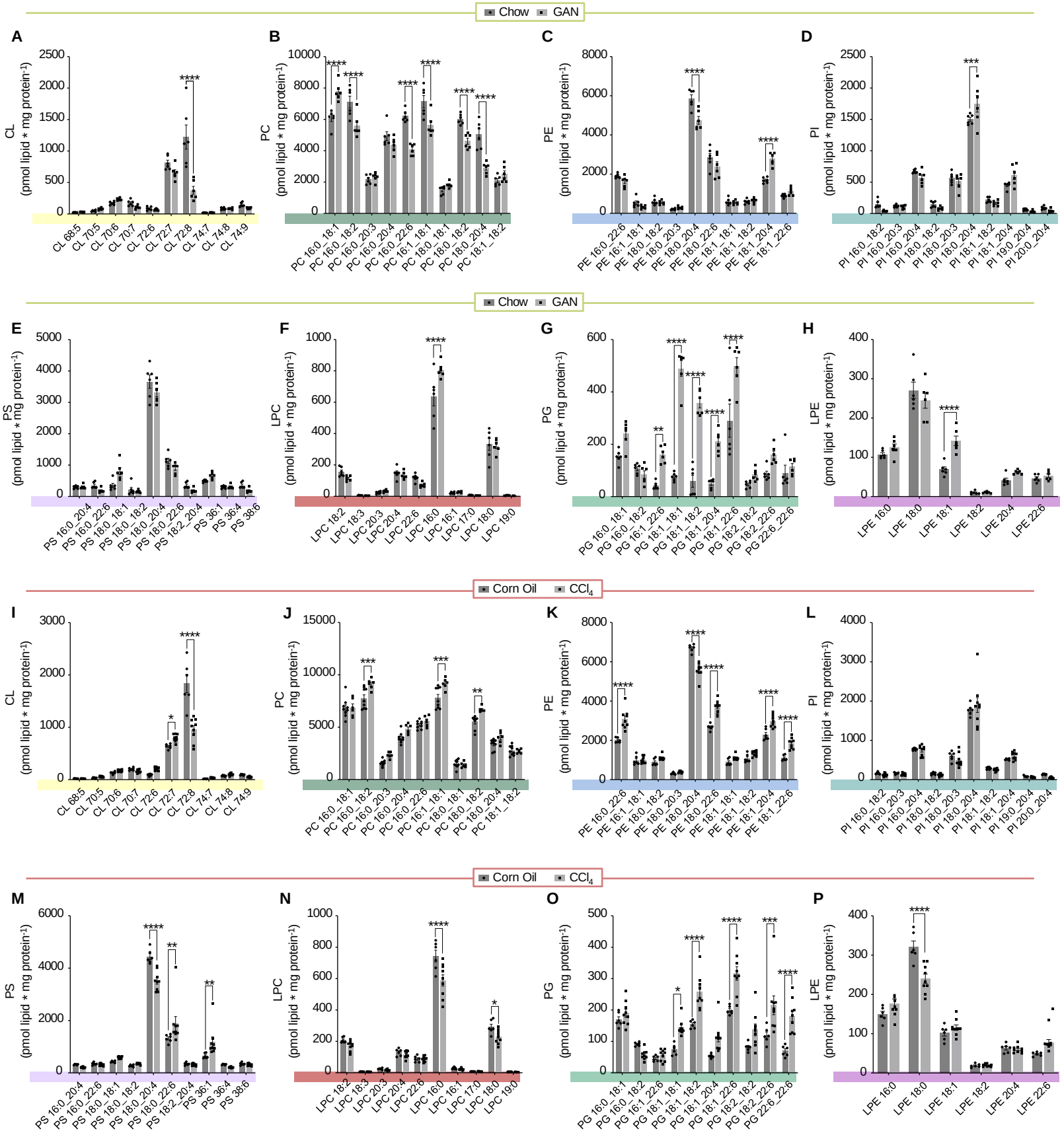

Supplemental Figure S3

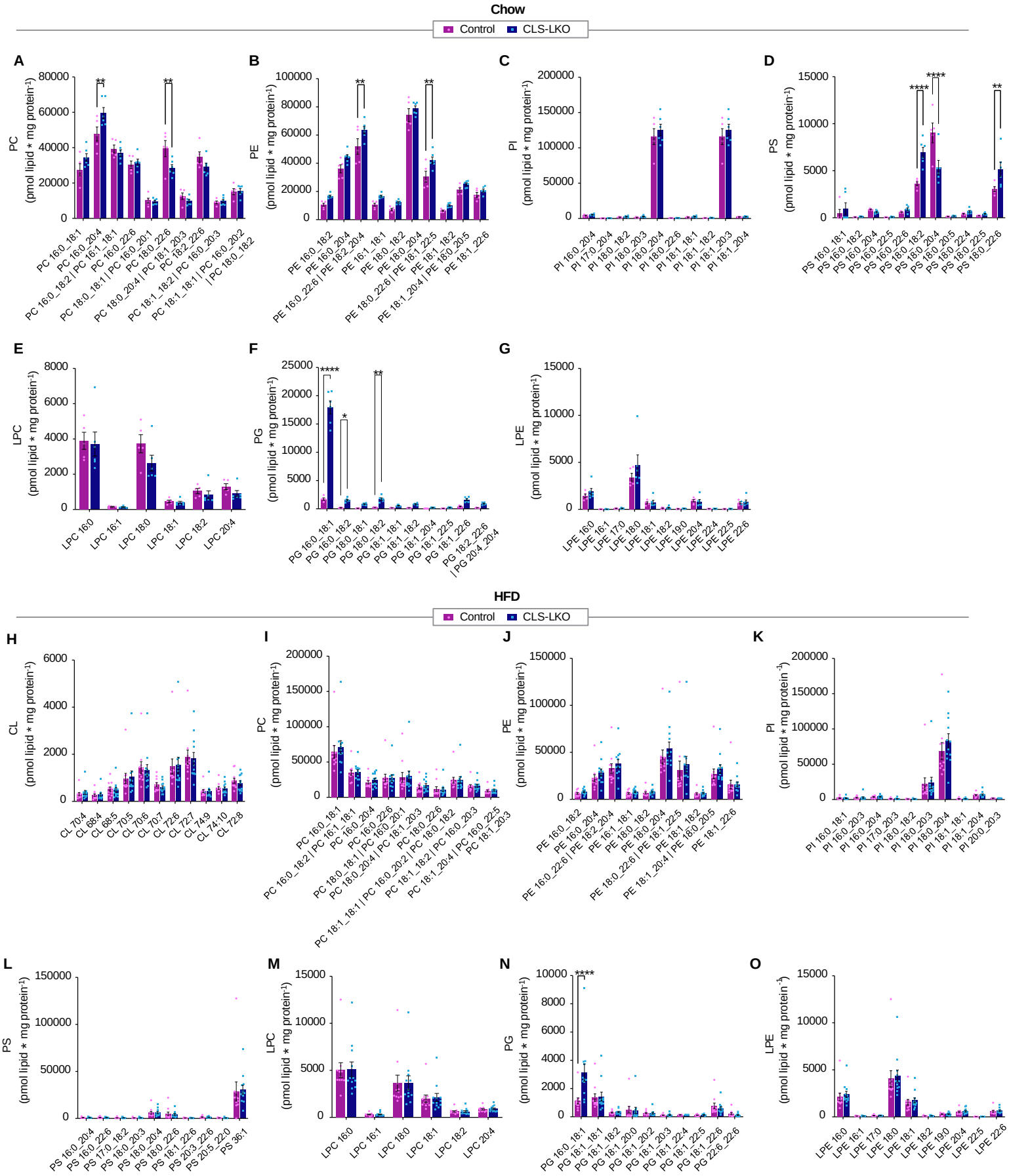

Supplemental Figure S4

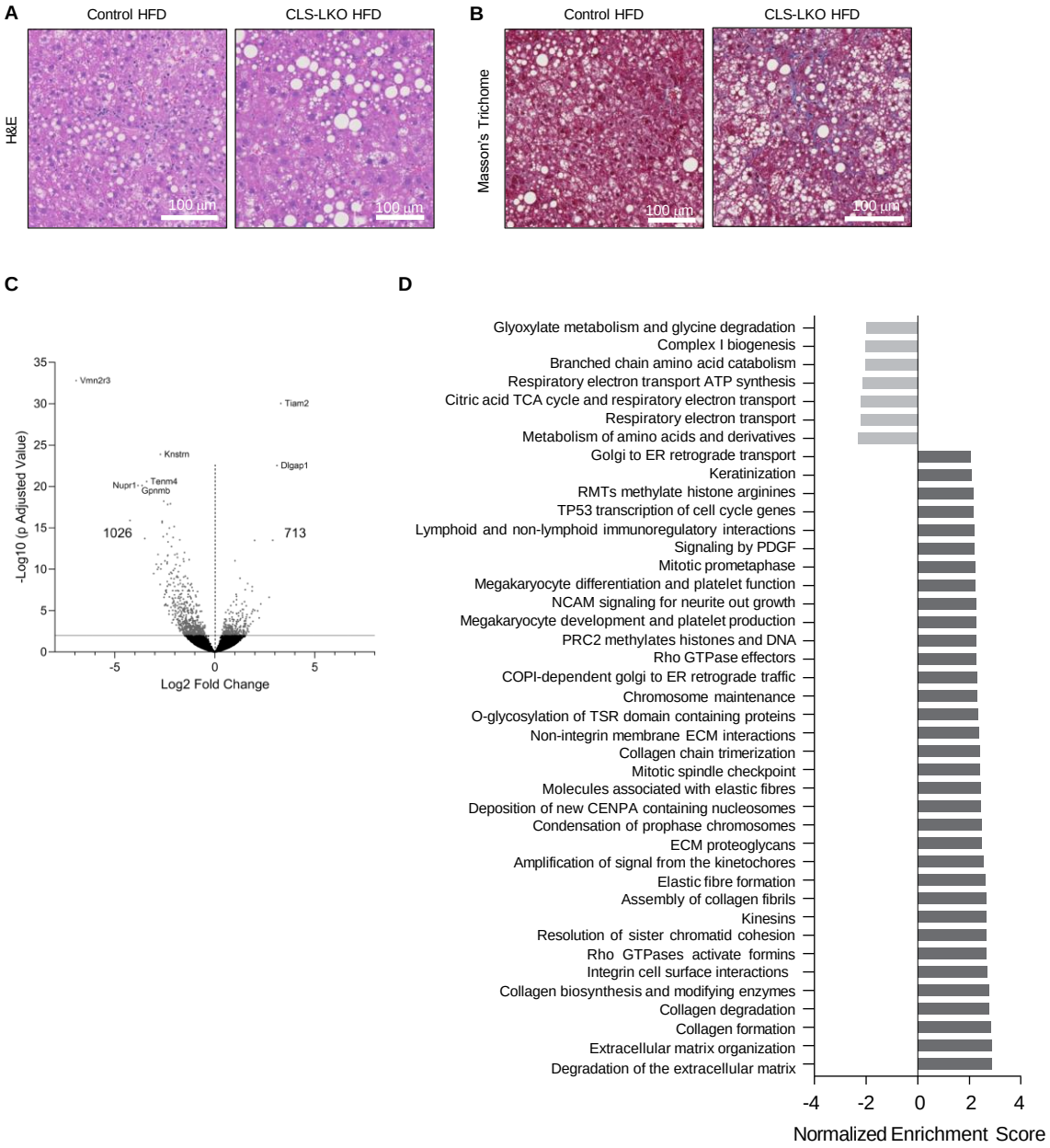

Supplemental Figure S5

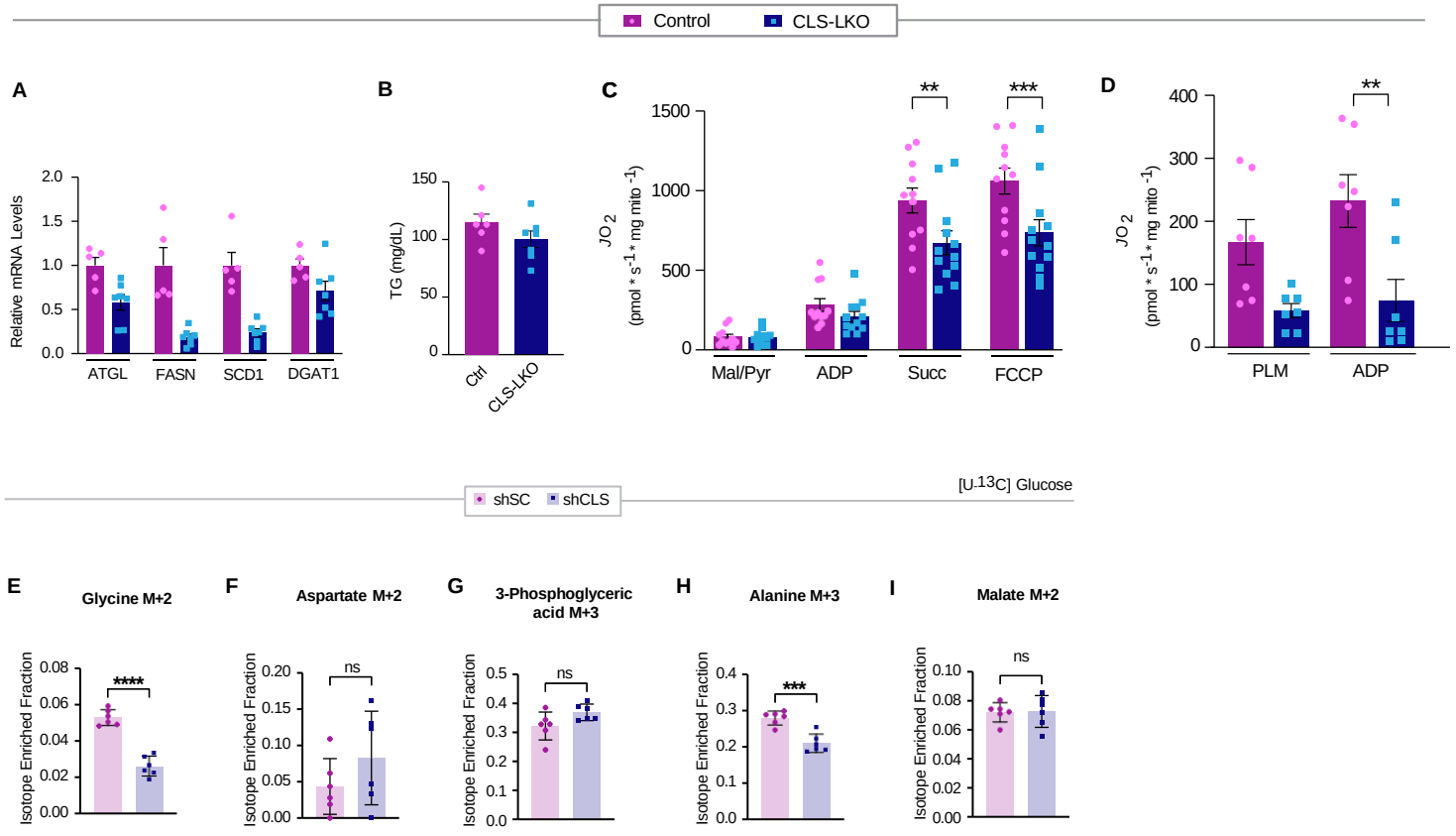

Supplemental Figure S6

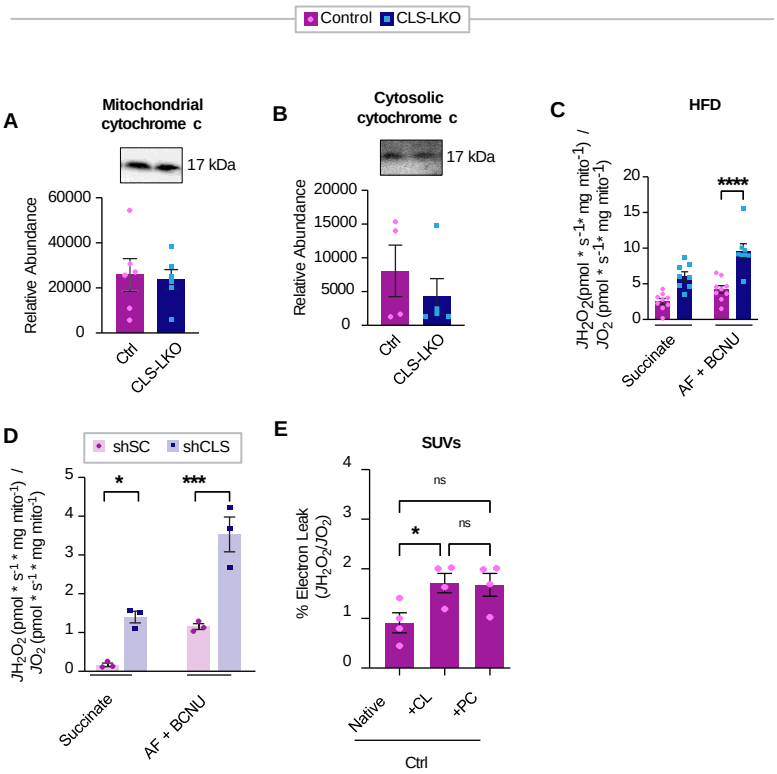

Supplemental Figure S7

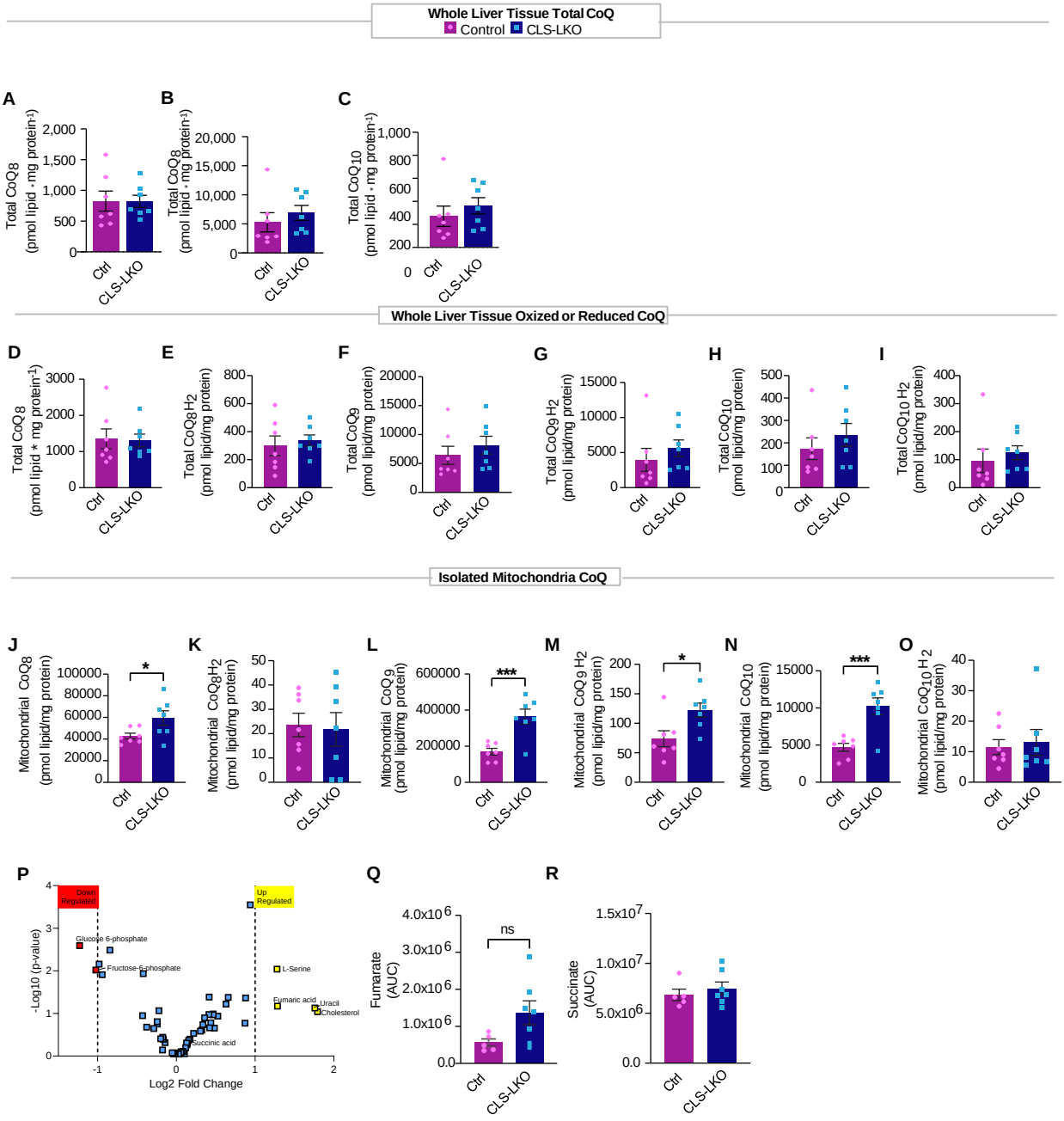

Key Resource Table

REAGENT or RESOURCE	SOURCE	IDENTIFIER
Antibodies		
GRIM19	Abcam	ab110240
SDHA	Abcam	ab14715
UQCRFS1	Abcam	ab14746
MTCO1	Abcam	ab14705
ATP5a	Abcam	Ab14748
NDUFA9	Abcam	Ab14713
Total OxPhos Antibody cocktail	Abcam	MS604-300
Citrate Synthetase	Abcam	Ab96600
Cytochrome c	Cell Signaling	11940S
Caspase-3	Cell Signaling	9661S
Caspase-7	Cell Signaling	9491S
Bacterial and virus strains		
Second-generation lentiviral-mediated knockdown system		
NEB Stable Competent E. Coli	NEB	C3040H
Biological samples		
Chemicals, peptides, and recombinant proteins		
Amplex Red Reagent	ThermoFisher Scientific	A12222
Auranofin	Sigma Aldrich	A6733
Carmustine (BCNU)	Sigma Aldrich	C0400
SPLASH Mix	Avanti Polar Lipids	330707
Cardiolipin Mix I	Avanti Polar Lipids	LM6003
Bovine Serum Albumin	Sigma Aldrich	A7030
Protease Inhibitor Cocktail	Thermo Scientific	78446
Tamoxifen	Sigma Aldrich	T5648
Sunflower Oil	Sigma Aldrich	S5007
TRIzol	Thermo Scientific	15596018
Mini-PROTEAN TGX Gels	BioRad	4561086
ECL	PerkinElmer	104001EA
Malate	Sigma Aldrich	M7397
Pyruvate	Sigma Aldrich	P2256
GDP	Sigma Aldrich	G7127
CL 316,243	Sigma Aldrich	C5976
ADP	Sigma Aldrich	A5285

ATP	Sigma Aldrich	A9187
Glutamate	Sigma Aldrich	G5889
Succinate	Sigma Aldrich	S3674
Carnitine	Sigma Aldrich	8.40092
Palmitoyl-CoA	Sigma Aldrich	P9716
Palmitoyl-L-carnitine	Sigma Aldrich	P1645
SYBR Green	Thermo Scientific	A25776
4% Paraformaldehyde	Thermo	J19943-K2
Opti-MEM	Gibco	31985
DMEM	Gibco	1195-092
FBS	Gibco	10082-147
Penicillin-streptomycin	Gibco	15140122
Critical commercial assays		
Pierce BCA Protein Assay Kit	Thermo Scientific	23227
iScript cDNA Synthesis Kit	BioRad	1708891
Deposited data		
Experimental models: Cell lines		
HEK293T cells	ATCC	CTRL-3216
Hepa 1-6 murine hepatoma cells	ATCC	CRL-1830
Experimental models: Organisms/strains		
Mouse: CLS conditional knockout (CLS-cKO)	Sustarsic et al. 2018	N/A
Mouse: CLS-LKO	This paper	N/A
Mouse: Alb-Cre	Jackson Laboratory	003574
Oligonucleotides		
RT qPCR Primer ATGL F (CCACTCACATCTACGGAGCC)	www.IDTDNA.com	
RT qPCR Primer ATGL R (TAATGTTGGCACCTGCTTCA)	www.IDTDNA.com	
RT qPCR Primer DGAT1 F (GACGGCTACTGGGATCTGA)	www.IDTDNA.com	
RT qPCR Primer DGAT1 R (TCACAACACACCAATTCAGG)	www.IDTDNA.com	
RT qPCR Primer FAS F (GGATAGCTGTGTAGTGTAACCAT)	www.IDTDNA.com	
RT qPCR Primer FAS R (GGTCATCGTGATAACCACACA)	www.IDTDNA.com	
RT qPCR Primer SCD1 F (GCTCTACACCTGCCTCTTCG)	www.IDTDNA.com	

RT qPCR Primer SCD1 R (CAGCCGAGCCTTGTAAGTTC)	www.IDTDNA.com	
RT qPCR Primer CLS F (TGACCTATGCAGATCTTATTCCA)	Johnson et al. 2019	
RT qPCR Primer CLS R (TGGCAGAGTTCGGTATCTGA)	Johnson et al. 2019	
RT qPCR Primer TNFa F (CCACCACGCTCTTCTGTCTAC)	www.IDTDNA.com	
RT qPCR Primer TNFa R (AGGGTCTGGGCCATAGAACT)	www.IDTDNA.com	
RT qPCR Primer Taz F (CCCTCCATGTGAAGTGGCCATTCC)	Johnson et al. 2019	
RT qPCR Primer Taz R (TGGTGGTTGGAGACGGTGATAAGG)	Johnson et al. 2019	
mtDNA F: (TTAAGACACCTTGCCTAGCCACAC)	Mouse Primer Depot NCI/NIH	
mtDNA R: (CGGTGGCTGGCACGAAATT)	Mouse Primer Depot NCI/NIH	
nucDNA F: (ATGACGATATCGCTGCGCTG)	Mouse Primer Depot NCI/NIH	
nucDNA R: (TCACTTACCTGGTGCCTAGGGC)	Mouse Primer Depot NCI/NIH	
Recombinant DNA		
Sc	Addgene	1864
Crls1	Sigma Aldrich	TRCN0000123937
psPAX2	Addgene	12260
pMD2.G	Addgene	12259
Software and algorithms		
GraphPad Prism 9.0	GraphPad	N/A
Other		

Supplemental Table S1.

Patient demographic information

	Healthy	MASH
Age at time of collection	50.3 ± 9.6 yrs	62.2 ± 7.1 yrs
Sex	Male: 1 Female: 10	Male: 9 Female: 8
Alcohol use?	N/A	Yes: 0 No: 17
Race	White: 9 African American: 1 Asian: 1	White: 10 Unknown: 7

Supplemental Figure Legends

Figure S1. Mitochondrial phospholipidome from Figure 1I and 1J.

(A) Abundance of mitochondrial CL species in liver of control mice or mice fed a HFD for 16 weeks (n=5 per group).

(B) Abundance of mitochondrial PC species in liver of control mice or mice fed a HFD for 16 weeks (n=5 per group).

(C) Abundance of mitochondrial PE species in liver of control mice or mice fed a HFD for 16 weeks (n=5 per group).

(D) Abundance of mitochondrial PI species in liver of control mice or mice fed a HFD for 16 weeks (n=5 per group).

(E) Abundance of mitochondrial PS species in liver of control mice or mice fed a HFD for 16 weeks (n=5 per group).

(F) Abundance of mitochondrial LPC species in liver of control mice or mice fed a HFD for 16 weeks (n=5 per group).

(G) Abundance of mitochondrial PG species in liver of control mice or mice fed a HFD for 16 weeks (n=5 per group).

(H) Abundance of mitochondrial LPE species in liver of control mice or mice fed a HFD for 16 weeks (n=5 per group).

(I) Abundance of mitochondrial CL species in liver from control mice or leptin-deficient mice, 30 weeks old (n=6 per group).

(J) Abundance of mitochondrial PC species in liver from control mice or leptin-deficient mice, 30 weeks old (n=6 per group).

(K) Abundance of mitochondrial PE species in liver from control mice or leptin-deficient mice, 30 weeks old (n=6 per group).

(L) Abundance of mitochondrial PI species in liver from control mice or leptin-deficient mice, 30

weeks old (n=6 per group).

(M) Abundance of mitochondrial PS species in liver from control mice or leptin-deficient mice, 30 weeks old (n=6 per group).

(N) Abundance of mitochondrial LPC species in liver from control mice or leptin-deficient mice, 30 weeks old (n=6 per group).

(O) Abundance of mitochondrial PG species in liver from control mice or leptin-deficient mice, 30 wks old (n=6 per group).

(P) Abundance of mitochondrial LPE species in liver from control mice or leptin-deficient mice, 30 wks old (n=6 per group).

Figure S2. Mitochondrial phospholipidome from Figure 1K and 1L.

(A) Abundance of mitochondrial CL species in livers from mice injected with corn oil or carbon tetrachloride for 10 wks (n=5 and 7 per group).

(B) Abundance of mitochondrial PC species in livers from mice injected with corn oil or carbon tetrachloride for 10 wks (n=5 and 7 per group).

(C) Abundance of mitochondrial PE species in livers from mice injected with corn oil or carbon tetrachloride for 10 wks (n=5 and 7 per group).

(D) Abundance of mitochondrial PI species in livers from mice injected with corn oil or carbon tetrachloride for 10 wks (n=5 and 7 per group).

(E) Abundance of mitochondrial PS species in livers from mice injected with corn oil or carbon tetrachloride for 10 wks (n=5 and 7 per group).

(F) Abundance of mitochondrial LPC species in livers from mice injected with corn oil or carbon tetrachloride for 10 wks (n=5 and 7 per group).

(G) Abundance of mitochondrial PG species in livers from mice injected with corn oil or carbon tetrachloride for 10 wks (n=5 and 7 per group).

(H) Abundance of mitochondrial LPE species in livers from mice injected with corn oil or carbon

tetrachloride for 10 wks (n=5 and 7 per group).

(I) Abundance of mitochondrial CL species in livers from mice fed the Gubra-Amylin MASH diet or chow for 30 wks (n=6 per group).

(J) Abundance of mitochondrial PC species in livers from mice fed the Gubra-Amylin MASH diet or chow for 30 wks (n=6 per group).

(K) Abundance of mitochondrial PE species in livers from mice fed the Gubra-Amylin MASH diet or chow for 30 wks (n=6 per group).

(L) Abundance of mitochondrial PI species in livers from mice fed the Gubra-Amylin MASH diet or chow for 30 wks (n=6 per group).

(M) Abundance of mitochondrial PS species in livers from mice fed the Gubra-Amylin MASH diet or chow for 30 wks (n=6 per group).

(N) Abundance of mitochondrial LPC species in livers from mice fed the Gubra-Amylin MASH diet or chow for 30 wks (n=6 per group).

(O) Abundance of mitochondrial PG species in livers from mice fed the Gubra-Amylin MASH diet or chow for 30 wks (n=6 per group).

(P) Abundance of mitochondrial LPE species in livers from mice fed the Gubra-Amylin MASH diet or chow for 30 wks (n=6 per group).

Figure S3. Mitochondrial phospholipidome from standard chow or high-fat diet fed control and CLS-LKO livers.

(A) Abundance of mitochondrial PC species in liver from control or CLS-LKO mice, 8 wks old (n=5 and 6 per group).

(B) Abundance of mitochondrial PE species in liver from control or CLS-LKO mice, 8 wks old (n=5 and 6 per group).

(C) Abundance of mitochondrial PI species in liver from control or CLS-LKO mice, 8 wks old (n=5 and 6 per group).

(D) Abundance of mitochondrial PS species in liver from control or CLS-LKO mice, 8 wks old (n=5 and 6 per group).

(E) Abundance of mitochondrial LPC species in liver from control or CLS-LKO mice, 8 wks old (n=5 and 6 per group).

(F) Abundance of mitochondrial PG species in liver from control or CLS-LKO mice, 8 wks old (n=5 and 6 per group).

(G) Abundance of mitochondrial LPE species in liver from control or CLS-LKO mice, 8 wks old (n=5 and 6 per group).

(H) Abundance of mitochondrial CL species in liver from control or CLS-LKO mice fed a high-fat diet for 8 wks (n=11 and 12 per group).

(I) Abundance of mitochondrial PC species in liver from control or CLS-LKO mice fed a high-fat diet for 8 wks (n=11 and 12 per group).

(J) Abundance of mitochondrial PE species in liver from control or CLS-LKO mice fed a high-fat diet for 8 wks (n=11 and 12 per group).

(K) Abundance of mitochondrial PI species in liver from control or CLS-LKO mice fed a high-fat diet for 8 wks (n=11 and 12 per group).

(L) Abundance of mitochondrial PS species in liver from control or CLS-LKO mice fed a high-fat diet for 8 wks (n=11 and 12 per group).

(M) Abundance of mitochondrial LPC species in liver from control or CLS-LKO mice fed a high fat diet for 8 wks (n=11 and 12 per group).

(N) Abundance of mitochondrial PG species in liver from control or CLS-LKO mice fed a high-fat diet for 8 wks (n=11 and 12 per group).

(O) Abundance of mitochondrial LPE species in liver from control or CLS-LKO mice fed a high fat diet for 8 wks (n=11 and 12 per group).

Figure S4. Additional histological and transcriptomic data from control and CLS-LKO mice.

(A) H&E stains for control and CLS-LKO mice fed a HFD for 8 wks.

(B) Masson's Trichrome stains for control and CLS-LKO mice fed a HFD for 8 wks.

(C) Volcano plot of genes differentially expressed in livers taken from control and CLS-LKO mice (n=5 and 7 per group).

(D) Normalized enrichment scores in RNA sequencing using Reactome database for most significantly affected pathways in livers taken from control and CLS-LKO mice (n=5 and 7 per group).

Figure S5. Additional metabolic, mitochondrial, and fluxomic phenotyping data with CLS deletion.

(A) Relative mRNA levels of lipogenic genes in livers from control and CLS-LKO mice (n=6 and 7 per group).

(B) Serum triglycerides for control and CLS-LKO mice (n=6 and 7 per group).

(C) JO_2 consumption in isolated liver mitochondria from control or CLS-LKO mice fed a Western HFD for 8 wks in response to 0.5 mM malate, 5 mM pyruvate, 2.5 mM ADP, 10 mM succinate, and 1.5 μM FCCP (n=11 and 12 per group).

(D) JO_2 consumption in isolated liver mitochondria from control or CLS-LKO mice fed a Western HFD for 8 wks in response to 0.02 mM palmitoyl-carnitine, 5 mM L-carnitine, and 2.5 mM ADP (n=7 per group).

(E) Levels of labeled glycine from glucose tracing in hepa1-6 cells (n=6 for shSC and shCLS).

(F) Levels of labeled aspartate from glucose tracing in hepa1-6 cells (n=6 for shSC and shCLS).

(G) Levels of labeled 3-phosphoglyceric acid from glucose tracing in hepa1-6 cells (n=6 for shSC and shCLS).

(H) Levels of labeled alanine from glucose tracing in hepa1-6 cells (n=6 for shSC and shCLS).

(I) Levels of labeled malate from glucose tracing in hepa1-6 cells (n=6 for shSC and shCLS).

Figure S6. Additional mitochondrial phenotyping data with CLS deletion.

(A) Western blot of cytochrome c levels in isolated mitochondria from HFD-fed control and CLS-LKO mice (n=6 per group).

(B) Western blot of cytochrome c levels in cytosolic fractions from HFD-fed control and CLS-LKO mice (n=6 per group).

(C) H_2O_2 emission and production in isolated liver mitochondria from control or CLS-LKO mice fed a Western HFD, stimulated with succinate, or succinate and auranofin and BCNU (n=9 and 8 per group).

(D) H_2O_2 emission and production in isolated liver mitochondria from hepa1-6 CLS knockdown cells stimulated with succinate, or succinate and auranofin and BCNU (n=3 per group).

(E) Quantification of electron leak using SUV to enrich mitochondria in control mice (n=4 per group).

Figure S7. Additional data on coenzyme Q

(A) Mass spectrometric analysis of total CoQ_8 levels in whole liver tissue from control and CLS-LKO mice (n=7 per group).

(B) Mass spectrometric analysis of total CoQ_9 levels in whole liver tissue from control and CLS-LKO mice (n=7 per group).

(C) Mass spectrometric analysis of total CoQ_{10} levels in whole liver tissue from control and CLS-LKO mice (n=7 per group).

(D) Oxidized CoQ_8 levels in whole liver tissue from control and CLS-LKO livers (n=7 per group).

(E) Reduced CoQ_8 levels in whole liver tissue from control and CLS-LKO livers (n=7 per group).

(F) Oxidized CoQ_9 levels in whole liver tissue from control and CLS-LKO livers (n=7 per group).

(G) Reduced CoQ_9 levels in whole liver tissue from control and CLS-LKO livers (n=7 per group).

(H) Oxidized CoQ_{10} levels in whole liver tissue from control and CLS-LKO livers (n=7 per group).

(I) Reduced CoQ_{10} levels in whole liver tissue from control and CLS-LKO livers (n=7 per group).

(J) Oxidized CoQ_8 levels in isolated mitochondria from control and CLS-LKO livers (n=7 per group).

(K) Reduced CoQ_8 levels in isolated mitochondria from control and CLS-LKO livers (n=7 per group).

(L) Oxidized CoQ_9 levels in isolated mitochondria from control and CLS-LKO livers (n=7 per group).

(M) Reduced CoQ_9 levels in isolated mitochondria from control and CLS-LKO livers (n=7 per group).

(N) Oxidized CoQ_{10} levels in isolated mitochondria from control and CLS-LKO livers (n=7 per group).

(O) Reduced CoQ_{10} levels in isolated mitochondria from control and CLS-LKO livers (n=7 per group).

(P) Volcano plot from untargeted metabolomics showing differential abundance of TCA cycle metabolites.

(Q) Fumarate levels from metabolomics data (n=5 and 7 per group).

(R) Succinate levels from metabolomics data (n=5 and 7 per group).

metabolites in CLS-LKO livers compared to controls (n=5 and 7 per group).